# X-ray Diffraction Reconstruction of the Inverted Hexagonal ($H_{II}$) Phase in Lipid–Water Systems†

David C. Turner‡ and Sol M. Gruner*

*Department of Physics, Joseph Henry Laboratories, Princeton University, Princeton, New Jersey 08544*

*Received May 1, 1991; Revised Manuscript Received October 28, 1991*

ABSTRACT: The structure of the inverted hexagonal ($H_{II}$) phase in biological lipid–water systems is studied to examine the physical interactions which drive the polymorphic phase behavior and which are also thought to play a relevant role in biological membrane function. A method is derived which yields the complex phase factors of the $H_{II}$ phase diffraction amplitudes from examination of a single sample. This method is applied to a low-resolution Fourier reconstruction of the $H_{II}$ phase in dioleoylphosphatidylethanolamine (DOPE) + water, specifically to examine deviations from the presumed circular model of the $H_{II}$ phase. It is found that the average radius of the water core, $R_w$, as determined from a Fourier reconstruction, is in good agreement with previously measured values of $R_w$ obtained from more time-consuming traditional methods [Tate, M. W., & Gruner, S. M. (1989) *Biochemistry 28*, 4245]. In addition to the average value of $R_w$, the Fourier reconstruction also can be used to determine the true shape of the water core. It is found that the water core is circular to within 5% of $R_w$ when the unit cell size is less than ~75 Å. Above 75 Å, however, a definite shape deformation becomes apparent, with radial noncircularities of 5–10%, probably in response to the increased entropic cost of packing the hydrocarbon chains into the anisotropic environment of the $H_{II}$ unit cell [Kirk, G. L., Gruner, S. M., & Stein D. E. (1984) *Biochemistry 23*, 1093]. As a more direct probe of the packing anisotropy, Fourier reconstructions of DOPE + dodecane and DOPE + squalene systems were compared with the reconstruction of DOPE. These oils are known to promote the low temperature occurrence of the $H_{II}$ phase, presumably by a reduction in the hydrocarbon packing stress. In support of this hypothesis, the alkanes were observed to relax the water core to a circular shape for even large lattices. In addition, anisotropy of the electron density near the end of the lipid chains is reduced when alkane is added, implying a more uniform hydrocarbon packing environment, consistent with the results of neutron diffraction upon the addition of deuterated decane [Turner, D. C., Gruner, S. M., & Huang, J. (1992) *Biochemistry* (following paper in this issue)].

A large fraction of the individual polar and charged lipid species in biological membranes form nonlamellar liquid-crystalline phases when dispersed in water (Cullis et al., 1985); the most common of these phases is the inverted hexagonal ($H_{II}$) phase (Figure 1a). In addition to forming in binary lipid–water systems, formation of the $H_{II}$ phase can be promoted by the addition of a small fraction of free hydrocarbon (~5 wt %) such as dodecane or squalene to form a ternary system (Kirk & Gruner, 1985; Sjölund et al., 1987, 1989; Siegel et al., 1989). For such a small volume of added alkane, however, the ternary system may be viewed as a slight perturbation of the binary system composition. The physical principles which lead to the formation of the $H_{II}$ phase in either of these systems may be important for understanding the role of nonlamellar forming lipids in a biological membrane; that is, the interactions causing the formation of the $H_{II}$ phase are also present in the bilayer configuration (Gruner, 1989; Tate et al., 1991). For example, the bilayer may be storing elastic energy which may affect biological membrane characteristics. These elastic contributions may be determined by examining the nonlamellar phases in general, and the $H_{II}$ phase specifically (Rand et al., 1990).

The $H_{II}$ phase is normally assumed to organize into cylindrical water cores surrounded by a lipid–hydrocarbon matrix (Luzzati & Husson, 1962; Luzzati, 1968). Several investigations of the $H_{II}$ lattice as a function of temperature and composition have described the average water-core radius and lipid thickness based on the assumption of circular symmetry (Seddon et al., 1984; Tate & Gruner, 1989). It has been speculated, however, that the water cores are likely to deviate from a circular shape (Kirk & Gruner, 1985; Tate, 1987; Seddon, 1990) and also that the hydrocarbon chains are not uniformly distributed near the boundary of the Wigner–Seitz cell (Kirk et al., 1984; Kirk & Gruner, 1985). Both types of anisotropy are likely to contribute an unfavorable entropic term to the overall free energy difference between the $H_{II}$ phase and the lamellar phase (Figure 1b). The addition of a small amount dodecane or squalene is thought to relieve the packing stress and possibly reduce the anisotropy in the unit cell (Kirk & Gruner, 1985; Gruner, 1989).

In this paper we describe an electron density reconstruction of the $H_{II}$ phase in 1,2-dioleoyl-*sn*-glycero-3-phosphoethanolamine (DOPE,[1] also called dioleoylphosphatidylethanolamine) from which the departure of the real unit cell from the cylindrical model is determined. Although several electron density reconstructions of the $H_{II}$ phase may be found

† D.C.T. was partially supported by a Garden State Graduate fellowship and an NIH cell biology training grant. Lipid research at Princeton University is supported by grants from DOE (DE-FG02-87ER60522), NIH (GM32614), and ONR (N00014-90-J-1702).

* To whom correspondence should be addressed.

‡ Current address: Naval Research Laboratories, Code 6090, Washington, D.C. 20375.

[1] Abbreviations: DOPE, dioleoylphosphatidylethanolamine; $L_\alpha$, lamellar liquid-crystal phase; $H_{II}$, inverted hexagonal phase; TLC, thin layer chromatography; $T_{bh}$, $L_\alpha$–$H_{II}$ transition temperature.

0006-2960/92/0431-1340$03.00/0 © 1992 American Chemical Society

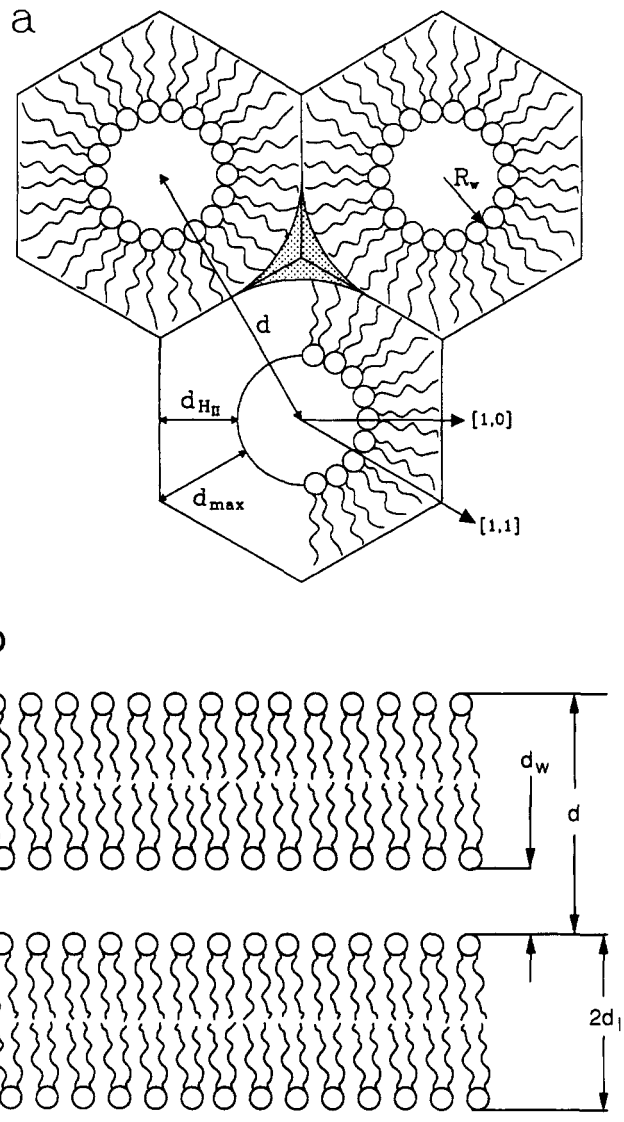


FIGURE 1: (a) Cross section of the $H_{II}$ phase showing the basis vector length or $d$-spacing, $d$, the extreme lipid lengths, $d_{max}$ and $d_{H_{II}}$, and the radius of the water core, $R_w$. Arrows pointing along the [1,0] and [1,1] directions are shown along with the interstitial region (stippled) where the chains must stretch to reach, compared with their length along the [1,0] direction. (b) The lamellar phase, a stacked bilayer phase sandwiching intermediate water layers. Definitions of $d$-spacing, $d$, water layer thickness, $d_w$, and lipid monolayer thickness, $d_l$, are shown.

in the literature (Caron et al., 1974; Gulik et al., 1985, 1988), none explicitly examine this departure from circular symmetry. The distribution of electron density in the unit cell can be calculated from a Fourier series with the diffraction peak amplitudes as the Fourier components. A new method for determining the complex phase factors of the diffraction amplitudes in the $H_{II}$ phase is described, and this method is used to generate reconstructions of the unit cell as a function of temperature on single samples. From the reconstructions, the average radius of the water core ($R_w$; Figure 1a) is extracted and is shown to agree with previous measurements (Tate & Gruner, 1989). The water core shape is shown to become hexagonally distorted with increasing lattice unit cell size; however, when dodecane or squalene is added to the phase, the water core shape relaxes back to a circle. In addition, the non-circularly symmetric modulation of the electron density near the end of the lipid chains is shown to be dramatically reduced upon the addition of these free hydrocarbons. These changes are discussed regarding their affect on the overall free energy of the system.

## Materials and Methods

*Sample Preparation.* DOPE was purchased from Avanti Polar Lipids (Birmingham, AL). Before being used, the lipid stock was checked and found to be at least 99% pure by thin layer chromatography (TLC) in a solvent of 90:54:5.7:5.3 $CHCl_3$/MeOH/25% $NH_4OH$/$H_2O$. Dodecane ($C_{12}H_{26}$) was purchased from Eastman Kodak (Rochester, NY), and squalene [$CH_3[C(CH_3)=CHCH_2CH_2]_5C(CH_3)=C(CH_3)_2$] was purchased from Sigma Chemical (St. Louis, MO). Glass X-ray capillaries, 1.5 mm in diameter with wall thickness of 10 $\mu$m, were purchased from Charles Supper (Natick, MA) and used for all samples.

The DOPE + water samples were prepared by dissolving a few milligrams of lipid in cyclohexane and transferring the solution to a preweighed capillary which had previously been flame sealed at one end. The capillary was frozen to −80 °C and then placed under vacuum at ~0 °C for 3–5 h to lyophilize off the cyclohexane. The light, fluffy lipid powder that remained was weighed and mixed with a precise volume of deionized water transferred via a Hamilton microsyringe (Hamilton Co., Reno, NV). The open end of the capillary was then sealed with 5-min epoxy (Devcon, Danvers, MA). The following DOPE + hydrocarbon + excess water samples were prepared: DOPE + 5% dodecane, DOPE + 10% dodecane, DOPE + 16% dodecane, and DOPE + 10% squalene, where all percentages refer to weight fractions of the non-water part of the samples. For these samples, the lipid was lyophilized into a small flame-sealed glass tube, and the hydrocarbon was added until the proper weight fraction was achieved. A few microliters of water was subsequently added, and the contents were mechanically mixed by repeated withdrawals and extrusions from the tip of a 10-$\mu$L Drummond microdispenser (Drummond Scientific, Broomall, PA). Once thoroughly mixed, the lipid–hydrocarbon–water slurry was transferred to an X-ray capillary. More water was added to be certain the water was in excess (>50% water; bulk water was observed in equilibrium with the lipid–water aggregate) and the capillary was sealed with epoxy. Mechanical agitation was necessary to ensure uniform mixing of the hydrocarbon into the lipid. The samples were made with excess water (>50% w/w) so that the lattice could swell to its hydration limit. Once the sample was made, it was equilibrated and mixed until uniform in appearance. Spinning the sample in a bench top centrifuge alternately right side up and upside down was effective in mixing the sample, particularly if the lipid was in the $L_\alpha$ phase at the time. Stubborn DOPE samples were refrigerated in the lamellar phase for up to 2 weeks until they were uniform. After diffraction from the samples had been recorded, a selection of them were broken open and lipid purity was checked by TLC for the formation of degradation products. All samples were found to be better than 99% pure.

*Data Collection and Analysis.* Diffraction data were collected on the Princeton SIT and CCD beamlines. The SIT and CCD detectors are two-dimensional image-intensified TV-type detectors which are read out in slow scan mode [Gruner et al., 1982; Milch et al., 1982; see also Templer et al. (1988)]. Copper K$\alpha$ X-rays (wavelength = 1.54 Å) generated by a Rigaku RU-200 rotating anode source were focused by Franks optics through the sample capillary onto the detector. The beam had roughly $10^8$ X-rays $s^{-1}$ at the sample and was focused to a spot size of 0.4 mm by 2 mm. The sample temperature was maintained by a programmable thermoelectric-based temperature controller which was capable

Table I: Smoothed Diffraction Amplitudes vs Temperature and d-Spacing

| | temp (°C)/*d*-spacing (Å) | | | | | | | |
|---|---|---|---|---|---|---|---|---|
| reflection order | 80/64.23 | 70/65.77 | 60/67.40 | 50/69.19 | 40/71.02 | 30/73.27 | 20/75.81 | 10/78.43 |
| (1,0) | 1.002 | 0.997 | 0.987 | 0.972 | 0.952 | 0.923 | 0.885 | 0.841 |
| (1,1) | 0.756 | 0.785 | 0.813 | 0.841 | 0.867 | 0.895 | 0.922 | 0.947 |
| (2,0) | 0.660 | 0.679 | 0.697 | 0.714 | 0.729 | 0.745 | 0.759 | 0.770 |
| (2,1) | 0.002 | 0.032 | 0.062 | 0.094 | 0.125 | 0.161 | 0.200 | 0.238 |
| (3,0) | 0.088 | 0.112 | 0.136 | 0.159 | 0.181 | 0.205 | 0.229 | 0.251 |
| (2,2) | 0.146 | 0.157 | 0.165 | 0.170 | 0.172 | 0.170 | 0.162 | 0.150 |
| (3,1) | 0.134 | 0.139 | 0.141 | 0.142 | 0.141 | 0.137 | 0.131 | 0.122 |
| (4,0) | 0.046 | 0.040 | 0.034 | 0.027 | 0.020 | 0.011 | 0.001 | 0.000 |
| (3,2) | 0.000 | 0.000 | 0.005 | 0.017 | 0.033 | 0.058 | 0.091 | 0.130 |
| (4,1) | 0.000 | 0.000 | 0.009 | 0.024 | 0.043 | 0.069 | 0.102 | 0.139 |

of a slew rate of 2 °C $s^{-1}$ within the range −40–90 °C, to a final stability of ±0.5 °C. The diffraction images were digitized and stored on computer tape for further analysis.

Since intensity information was required for the Fourier reconstruction of the $H_{II}$ phase, a flat-field correction was done on the SIT camera before data was taken. A uniform X-ray source was used to calibrate out the nonuniformities across the detector face. Uncorrected images of the uniform source showed variations of up to 20%, while corrected images were flat to within 0.5%. All diffraction data files were flat-field corrected before any further intensity analysis was done. The specimen to detector distance was calibrated before each run with a lead stearate sample, which has a unit cell spacing of 47.46 Å at 20 °C.

The diffraction patterns were acquired every 10 °C from 10 to 80 °C. At each temperature the sample was allowed to equilibrate for 1 h before three 10-min exposures were taken followed by one 30-s exposure. The long exposures recorded the weak, high angle peaks, while the short exposure was necessary to avoid detector saturation of the stronger peaks. The diffraction signature of a hexagonal lattice is a set of peaks $(h,k)$ which index with ratios $(h^2 + hk + k^2)^{1/2}$, e.g., the first few peaks should index to 1, $\sqrt{3}$, 2, $\sqrt{7}$, 3, ..., etc. Once the diffraction pictures were acquired, they were digitized, flat-field corrected, and saved onto magnetic tape.

At each temperature the short and long exposures were scaled according to exposure time. The resulting powder diffraction patterns were then radially integrated (densitometerized) within an angle of ±20° to the lamellar axis and then merged. This integration of the diffraction pattern is called a "dens" plot (Figure 2). The unit cell spacing $d$, which is the inter-water core distance in the $H_{II}$ phase, is then determined by fitting the diffraction peaks to a hexagonal lattice. In a good sample, as many as 10 peaks can be seen [out to the (4,1) peak]. The integrals under the peaks were determined by fitting a series of Gaussians to the peaks with a quadratic baseline using a nonlinear least-squares method based on the Levenberg–Marquardt algorithm (Press et al., 1986). Specifically, each Gaussian was parameterized by a position, width, and amplitude; all peaks out to the (3,1) reflection could be easily fit by allowing each of the parameters to freely adjust. In some cases the (2,2) and (3,1) peak widths had to be constrained for a good fit because these closely spaced peaks were usually not well resolved from one another. If so, the peak widths were then determined from the trend seen in fits to the lower order reflections. The typical peak widths ranged from 3.7 pixels half-width at half-maximum for the (1,0) peak to around 4.4 for the (3,1) peak. The quality of the fit to background was one of the most important factors deciding whether to accept or reject a fit. The intensities of the (4,0), (3,2), and (4,1) reflections were usually very weak (Figure 2) and so were often not fit well by the fitting routine. In these cases their intensities were estimated from the peak height in relation to the amplitudes of the stronger reflections. The minimum intensity consistent with observed diffraction was used, and it should be noted that the intensities of these peaks may be uncertain by as much as 50%.

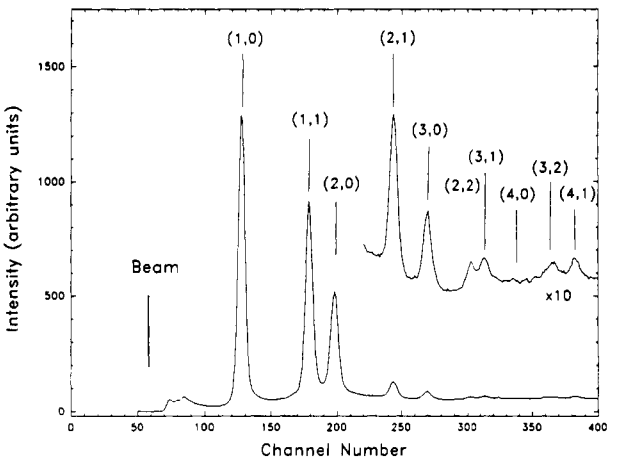


FIGURE 2: Angular integration or densitometerization (see text) of the two-dimensional diffraction pattern of DOPE at 10 °C, $d$ = 78.4 Å, including a ×10 blowup to show the weak lines at high angle. The numbered pairs index the reflections on a hexagonal reciprocal lattice.

The raw intensities were calibrated for multiplicity by dividing the intensities of the (2,1), (3,1), (3,2), and (4,1) peaks by 2. A Lorentz correction was applied by multiplying each peak intensity by sin $(\theta)$, since the sin $(2\theta)$ powder diffraction pattern Lorentz correction factor was previously accounted for by the angular densitometerization [see Warren (1969) for a discussion of the Lorentz correction]. Each peak intensity was then normalized to the intensity of the (1,0) peak at 80 °C, which is normally the strongest diffraction peak. Since the peak amplitudes are expected to change smoothly with temperature they were smoothed by a least-squares fitting procedure to a quadratic function of temperature. Table I shows corrected peak amplitudes and $d$-spacings for a DOPE + excess water sample at temperatures from 10 to 80 °C. The $d$-spacing is measured to ±0.5 Å, with the fall of $d$-spacing with temperature a characteristic of the $H_{II}$ phase. This data set was then used as the basis for all further analysis.

Reproducibility was measured by comparing the amplitudes derived from three different samples. Over all temperatures, the strong (1,0), (1,1), and (2,0) reflections agree to better than 5%, while the weaker (2,1), (3,0), (2,2), and (3,1) reflections agree to better than 10%. Much of this variation correlates with the small differences in $d$-spacings among the samples. The very weak (4,0), (3,2), and (4,1) were found to have a scatter of about 40%, which was a result of the way these amplitudes were estimated from the diffraction pattern. As described below, systematic checks were performed to assure that this scatter among the data sets did not influence the results presented later in the paper.

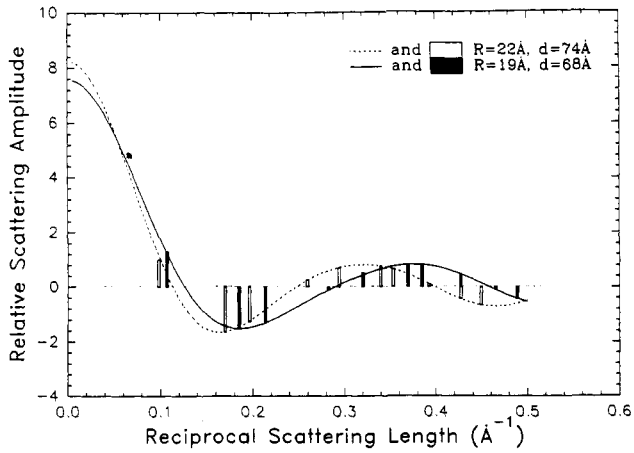


FIGURE 3: Structure factor for the $H_{II}$ phase, at two different water fractions, in the approximation of a simple circular model (see Figure 5). The abcissa is in units of $q = 4\pi \sin(\theta)/\lambda$, where $2\theta$ is the scattering angle and $\lambda$ is the X-ray wavelength in angstroms. The change in $d$ is assumed to be entirely due to the change in $R_w$. Unlike the lamellar case, the structure factor changes with water content along with the position of the peaks. The $d$ = 68 Å example has a phasing of +,–,–,–,+,+,+,+,–,–, while the $d$ = 74 Å example has a phasing of +,–,–,+,+,+,+,+,–,–.

*Phasing the Diffraction Amplitudes.* The electron density distribution within the unit cell is given by the Fourier transform of the diffracted structure factor function. In Bragg diffraction, the peak amplitudes sample the structure factor in such a way that the continuous structure factor cannot be observed. However, the structure factor is critically sampled so that the exact electron density distribution, up to a critical wavelength, within the unit cell can be determined with the diffraction peak amplitudes as the Fourier components, i.e., by application of the sampling theorem. Establishing the phases of these diffracted amplitudes has always been the main obstacle to obtaining Fourier reconstructions. Taking the square root of the intensity results directly in the magnitude of the structure factor; however, its phase remains unknown. In general, it may have an arbitrary complex phase factor $e^{i\alpha}$ described by the phase angle $\alpha$. The $H_{II}$ phase is centro- and mirror-symmetric, so the phase angle $\alpha$ can take only the values $\alpha = 0$ or $\pi$, which means the structure factor is real and we only need to find its sign.

The swelling method used for phasing lamellar systems (Perutz, 1954; Torbet & Wilkins, 1976; Franks, 1976) cannot be directly applied to the $H_{II}$ phase because changing the water content changes the overall distribution of matter in the unit cell, dramatically affecting the structure factor (Figure 3). In this paper we describe an extension to the method of Stamatoff and Krimm (1976) to the $H_{II}$ phase which can successfully find phase sets without relying on a cylindrically symmetric approximation. The method is robust and agrees well with less rigorous methods based on modeling and trial and error.

To begin, consider two inverted hexagonal phases H and H′ with slightly different water contents, with their lipid–water interface at $R_w$ and $R_w'$ and lattice repeat $d$ and $d'$, respectively. They are arranged so that H′ has slightly more water than H, with $R_w' > R_w$. We define the difference between the two radii to be $\delta$, such that $R_w + \delta = R_w'$, where $\delta$ is small compared to $R_w$. Now to relate the scattering density in H to the scattering density in H′, consider the scattering density at a given point $\mathbf{r}$ in unit cell H, $\rho_e(\mathbf{r})$. For small $\delta$, the scattering density in H′ at the point $\mathbf{r} + \delta$, $\rho'_e(\mathbf{r} + \delta)$ should be nearly the same as $\rho_e(\mathbf{r})$, where $\delta$ is always oriented in the radial direction. This assumption means that the water enters at the center of the water core and simply displaces everything radially outward without altering the structure significantly. It is similar to the assumption made for the swelling method in the lamellar phase but is much more dangerous because any significant increase in the water cylinder radius *will* change the structure of the unit cell. The trick is to pick the smallest $\delta$ which shows a measurable change in the diffracted intensities. As will be shown later, this is not a stringent requirement, since in most cases a shift of 5% in water cylinder radius will change the diffraction without destroying the correspondence between $\rho_e(\mathbf{r})$ and $\rho'_e(\mathbf{r} + \delta)$. Since the increase in unit cell size from H to H′ is assumed to be entirely due to swelling of the water cylinder, $2\delta = d_{H'} - d_H$ gives the value of $\delta$ directly.

Determining the proper phase set is now straightforward: simply compare $\rho_e(\mathbf{r})$ and $\rho'_e(\mathbf{r} + \delta)$ for each phase choice; the proper phase set will have the closest correspondence. Stamatoff and Krimm (1976) solved this problem for swelling in lamellar geometries, and it will be extended to the $H_{II}$ phase here. Since the Wigner–Seitz cell for the $H_{II}$ phase is centrosymmetric (and also reflection symmetric), the scattering density can be written as a simple Fourier cosine series:

$$\rho_e(x,y) = \frac{F(0)}{A} + \frac{1}{4A}\sum_{(i,j)\neq(0,0)} F_{ij} \cos(q_{ij_x}x) \cos(q_{ij_y}y) \quad (1)$$

where $\mathbf{r} = (x, y)$, $A$ is the area of the unit cell, $F_{ij}$ is the amplitude for the peak at position $q_{ij}$, and $i,j$ run over all of the positive integers {1, 2, 3, ...}. As in the lamellar case, the constant $F(0)$ is not directly measurable and simply results in a density offset, so we will ignore it and concentrate on the cosine series. Define the relative scattering density to be

$$\tilde{\rho}_e(x,y) = \frac{1}{4A}\sum_{(i,j)\neq(0,0)} F_{ij} \cos(q_{ij_x}x) \cos(q_{ij_y}y) \quad (2)$$

A way to measure the difference between $\rho_e$ and $\rho'_e$ is to calculate the mean square difference between them, integrated over the entire unit cell $H$. Accounting for possible differences in relative and absolute scaling, the deviation $\Delta$ is written

$$\Delta \equiv \frac{1}{A}\int\int_H [\tilde{\rho}'_e(\mathbf{r} + \delta) - C\tilde{\rho}_e(\mathbf{r}) - B]^2 \, d\mathbf{r} \quad (3)$$

where $C$ is a relative scaling constant between $\tilde{\rho}$ and $\tilde{\rho}'$ and $B$ is related to the difference between $F(0)$'s. Minimizing $\Delta$ with respect to $C$ and $B$ for each possible phase set results in a table of $\Delta$ vs phasing. The minimized expressions for $B$ and $C$ are

$$C = \left(A\int\int_H \tilde{\rho}'_e(\mathbf{r} + \delta)\tilde{\rho}_e(\mathbf{r}) \, d\mathbf{r} - \int\int_H \tilde{\rho}'_e(\mathbf{r} + \delta) \, d\mathbf{r} \times \int\int_H \tilde{\rho}_e(\mathbf{r}) \, d\mathbf{r}\right) \Big/ \left(A\int\int_H [\tilde{\rho}_e(\mathbf{r})]^2 \, d\mathbf{r} - \left[\int\int_H \tilde{\rho}_e(\mathbf{r}) \, d\mathbf{r}\right]^2\right) \quad (4)$$

$$B = \frac{1}{A}\left[\int\int_H \tilde{\rho}'_e(\mathbf{r} + \delta) \, d\mathbf{r} - C\int\int_H \tilde{\rho}_e(\mathbf{r}) \, d\mathbf{r}\right] \quad (5)$$

The phase set with the smallest $\Delta$ should be the correct phasing. The relative scaling of the two data sets ($C$) can be measured experimentally by determining the scattering power of the samples, which is defined as the fraction of beam that the sample diffracts out the main beam and is computed in practice by summing the intensities of all visible orders. The value of $C$ coming from the above fit should agree with the actual experimental scaling of the two data sets. For convenience, the data are always scaled such that $C \approx 1$. The proper phase set can be extracted from the table by the following procedure: (1) exclude all phase sets whose scale factor $C$ differs from 1 by more than 0.05, and (2) choose the set with the smallest $\Delta$ of those that remain. The value 0.05 was

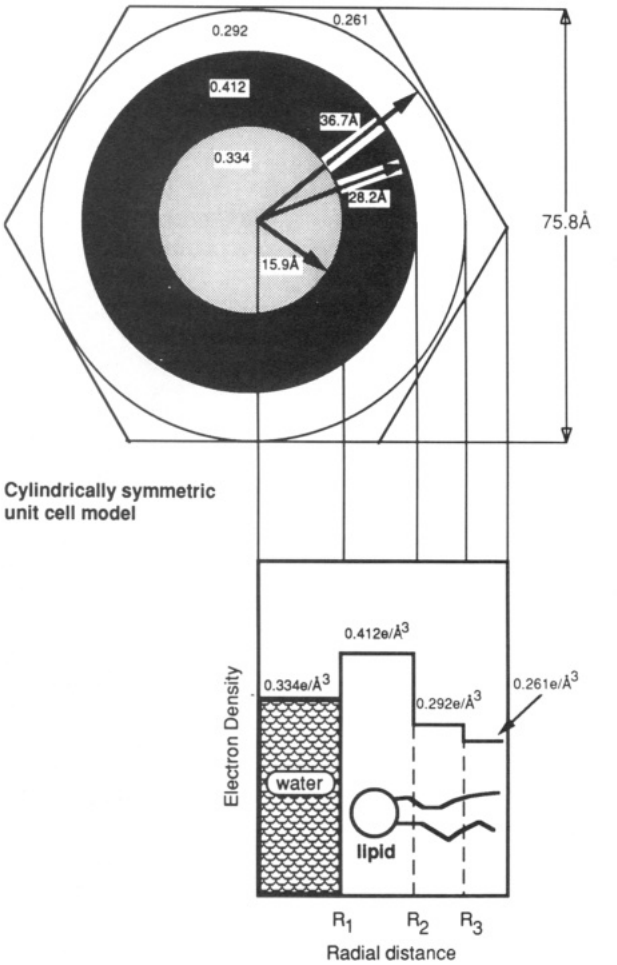


FIGURE 4: Cylindrically symmetric unit cell model of the Wigner–Seitz cell. The electron densities used are given in terms of number of electrons per Å$^3$ (e/Å$^3$). A characteristic radial slice is given which shows the approximate radial distribution of lipid and water.

determined empirically from several unit cell models as a comfortable limit to the variation in scaling. In other words, the prescription used for finding the proper phasing is to throw out all of the cases where $C$ is not in agreement with the data and then to pick the smallest $\Delta$ from the rest. For low-resolution reconstructions, the constant $B$ is difficult to interpret correctly and so will not be considered further.

Modeling shows that this approach works very well. The procedure for modeling was to use a simple model of the unit cell electron density distribution to generate a set of diffraction amplitudes and phases, such as that in Figure 4, and apply the above method to the amplitudes. This procedure has been carried out for several model systems with different values for the radius of the water core, and the phase set determined agrees with the actual phase set. The procedure appears to be robust, converging to the correct phase set even when white noise is added to the model amplitudes, as long as the overall trend in the amplitudes is preserved.

Since the above method is not foolproof (no phasing method is foolproof), many consistency checks are done. Those phase sets which are physically unreasonable are thrown out. These can include any phasing which results in an electron density profile inconsistent with the known overall composition of the unit cell. For example, we expect an electron-dense region near the lipid headgroup, an intermediate density in the water region, and a low-density region in the fatty acid hydrocarbon tail region. The structure is also subject to the constraint that it change smoothly with water concentration and temperature, which can be quite useful in eliminating unlikely phase sets. Finally, a model consistent with the data is very useful in determining both the phasing and the absolute electron density, along with a possible Debye–Waller disorder factor contribution, as will be described in the next section.

## Results

*Reconstructing the Unit Cell.* The 10 diffraction orders can have $2^9$ possible phasings, so initial reconstructions were derived from only the first few orders, usually 5, which reduces the number of phasings to 16 different possibilities. Electron density maps were made from all possible phase choices and compared with the expected gross features of the unit cell, particularly with respect to consistency with known electron density ratios of the water, phospholipid headgroup, and hydrocarbon. The electron densities for water and hydrocarbon were calculated directly from their mass densities (Weast, 1974) to be 0.334 e/Å$^3$ and 0.290 e/Å$^3$ at 20 °C, respectively, while the approximate electron density of the headgroup was taken to be ~0.410 e/Å$^3$ from lamellar reconstruction data (Franks et al., 1982), and the electron density of the terminal methyl group was taken to be 0.169 e/Å$^3$ (Knott & Shoenborn, 1986; Cabane, 1986). The number of peaks included in the fit determines the *resolution* of the reconstruction. This can be described as the convolution of the true electron density distribution with a resolution function (the Fourier transform of a cylinder function) which has a full width at half-maximum of $\Delta r = 3.8137/\pi q_{max}$, where $q_{max}$ is the cut-off frequency in reciprocal space. As an example, a 5-peak reconstruction of the $H_{II}$ phase in DOPE at 20 °C has $\Delta r \sim 26$ Å, while a 10-peak reconstruction has $\Delta r \sim 17$ Å. The low resolution of the 5-peak reconstruction actually makes it easier to differentiate among the possible phase choices because all fine detail is washed out, so most of the incorrect phasings give improbable structures. Only a few of the phasings were consistent with a water-in-oil structure. The proper phasing, +,–,–, is the only one consistent with the known partitioning of lipid and water within the unit cell. As an additional check, when the water core radius was changed via temperature or composition, the amplitude of a given peak changed smoothly and in some cases was seen to go through zero. In nearly every case this requires a change of phase so that structural trends within the unit cell continue smoothly across the zero. This can also be quite useful in eliminating unlikely phase sets. Once the phases for the first five peaks are established, the higher order peaks can be added one at a time, to judge their effect independently. These simple arguments made it possible to reduce the number of likely phasings of the first seven peaks to less than two or three combinations.

The swelling method described above corroborated the proposed phasing of the first seven peaks. Table II shows a ranking of the phase sets according to $\Delta$, generated from a comparison of the first seven amplitudes of DOPE in excess water at 20 and 30 °C. The unit cell size ($d$-spacing) was reduced by increasing the temperature of the sample. Tate and Gruner (1989) have shown that the change in $d$-spacing results primarily from a change in the water core radius. Since the electron density ratios of the constituents shift by less than 2% (as calculated from the change in mass densities) over a 10 °C temperture span, this is a very simple way of determining the phase set from a single excess water sample. In all cases, this method returned an unambiguous phase set for at least the first six or seven peak amplitudes. Determining the phasing of the last three peaks in the data is somewhat difficult. As might be expected, the swelling method is not particularly useful because of their small amplitudes, especially

Table II: Ranking of Phase Sets for DOPE Swelling from 30 to 20 °C[a]

| Δ | C | B | phasing |
|---|---|---|---|
| 0.000254 | 0.802761 | −0.000217 | +,+,+,+,+,+,+,+ |
| 0.001256 | 0.963447 | −0.000044 | +,−,−,+,+,+,− ← |
| 0.001907 | 0.826646 | −0.000227 | +,+,+,+,+,+,− |
| 0.002258 | 0.957266 | −0.000036 | +,−,−,+,+,+,+ ← |
| 0.002451 | 0.870960 | −0.000200 | +,+,+,−,+,+,− |
| 0.002663 | 0.957749 | −0.000023 | +,−,−,+,+,−,− |
| 0.003045 | 0.952938 | −0.000014 | +,−,−,+,+,−,+ |
| 0.003221 | 0.929424 | −0.000144 | +,+,−,−,+,+,− |
| 0.003582 | 0.890618 | −0.000174 | +,+,+,−,−,+,− |
| 0.003686 | 0.852663 | −0.000190 | +,+,+,−,+,+,+ |
| 0.004002 | 0.906109 | −0.000171 | +,+,−,+,+,+,− |
| 0.004115 | 0.931187 | −0.000123 | +,+,−,−,+,−,− |
| 0.004556 | 0.892855 | −0.000163 | +,+,−,+,+,+,+ |
| 0.004638 | 0.828647 | −0.000191 | +,+,+,+,−,+,+ |
| 0.004833 | 0.951183 | −0.000019 | +,−,−,+,−,+,− |
| 0.004903 | 0.921624 | −0.000135 | +,+,−,−,+,+,+ |
| 0.005184 | 0.848911 | −0.000201 | +,+,+,+,−,+,− |
| 0.005344 | 0.924817 | −0.000114 | +,+,−,−,+,−,+ |
| 0.005363 | 0.879168 | −0.000179 | +,+,+,−,+,−,− |
| 0.005410 | 0.948322 | −0.000010 | +,−,−,+,−,+,+ |
| 0.005745 | 0.875867 | −0.000165 | +,+,+,−,−,+,+ |
| 0.005788 | 0.816223 | −0.000197 | +,+,+,+,+,−,+ |

[a] The two best phase sets are pointed out with arrows.

in light of their large measurement errors (~40%). At this point, the only alternative method is modeling. The model predicts a set of amplitudes along with their phasing by simulating the electron density distribution in the unit cell. A crude starting model (see below) is refined until the best agreement with the experimental amplitudes is reached, usually by a type of least-squares algorithm. Modeling has long been used to fit lamellar diffraction data (Worthington, 1969; Worthington et al., 1973; Büldt et al., 1979; Weiner et al., 1989). In addition to simply determining the phasing of the diffraction peaks, modeling is also important for determining what kind of information can be reliably extracted from the reconstruction, particularly with respect to the influence of Fourier series cutoff artifacts.

*Modeling.* For simplicity, the initial models were made to be cylindrically symmetric. The unit cell was split up into four regions: water, phospholipid headgroup, bulk hydrocarbon region, and terminal methyl group region, as shown in Figure 4. The correct electron densities were arranged by adding uniform disks of the appropriate density. The Fourier transform of these disks is given by the function (Arfken, 1985)

$$F(q) = 2\pi\left[(\rho_w - \rho_{hg} - \rho_{hc} - \rho_{tm})\frac{R_1 J_1(qR_1)}{q} + (\rho_{hg} - \rho_{hc} - \rho_{tm})\frac{R_2 J_1(qR_2)}{q} + (\rho_{hc} - \rho_{tm})\frac{R_3 J_1(qR_3)}{q} + \rho_{tm}\delta^2(q-0)\right] \quad (6)$$

where $J_1$ is the first Bessel function of the first kind, $\rho_{tm}$ is the scattering density of the terminal methyl groups, $\rho_{hc}$ is the scattering density of the hydrocarbon region, $\rho_{hg}$ is the scattering density of the headgroup region, $\rho_w$ is the scattering density of the water region, $R_1$ is the inner radius of the headgroup region, $R_2$ is the outer radius of the headgroup region, and $R_3$ is the inner radius of the location of the terminal methyl group region (Figure 4). The uniform background density to which all the other densities were added, in this case $\rho_{tm}$, is only important at the origin of reciprocal space, so it need not be considered further. The values $\rho$ were calculated to be the same as the known electron densities of the regions, and the $R$'s were fit to the diffraction amplitudes with a least-squares algorithm.

Since these systems are soft, we expect thermal fluctuation and undulations to have important effects on the structure factor. Assuming a simple isotropic disorder within the sample, we get the standard Debye–Waller correction to the calculated structure factor, $F_f(\mathbf{q})$:

$$F_f(\mathbf{q}) = e^{[-(\mathbf{q}\cdot\zeta)^2]/2}F(\mathbf{q}) \quad (7)$$

where $F(\mathbf{q})$ is the ideal structure factor evaluated at momentum transfer $\mathbf{q}$ in reciprocal space and $\zeta$ is the characteristic mean square size of the fluctuation. This factor is also often written as $e^{-M}$ or $e^{-B\sin^2(\theta)/\lambda^2}$. The strong $\theta$ dependence diminishes the amplitudes of the high-angle diffraction peaks quickly. The model systems of the $H_{II}$ phase required a range of $B \approx 300$ Å$^2$ to $B \approx 390$ Å$^2$ for good agreement with the observed amplitudes, which corresponds to a mean square fluctuation of 4–5 Å$^2$, sharply in contrast to the 0.03–0.04 Å$^2$ typical of low molecular weight crystals (Woolfsen, 1970). These values are, however, consistent with previously published values for lamellar lipid phases (Franks et al., 1982).

It must be noted that this calculation of the Debye–Waller factor is only a crude approximation if the density fluctuations are spatially correlated or anisotropic within the unit cell. A calculation of these correlated fluctuations will not be described here, but we would expect a peak in reciprocal space at the wavelength of the fluctuations. Anisotropic disorder within the unit cell may also contribute to the observed diffraction pattern. In the $H_{II}$ phase this type of disorder could favor the on-axis peaks over the off-axis peaks and could possibly be confused with a non-circularly symmetric electron density in the unit cell. Modeling shows that anisotropic distortion can improve the fit to the diffraction data slightly; however, fitting a non-circularly symmetric unit cell electron density distribution improves the fit by nearly an order of magnitude. Therefore, for simplicity, we will stick with the form calculated above, noting that higher resolution studies will require a more sophisticated treatment of the thermal vibrational disorder.

Once a basic model is determined, the electron density ratios are optimized to give the best fit. The best fitting cylindrical models at 20, 50, and 80 °C are shown in Figure 5. Table III shows a comparison of the predicted amplitudes with the measured amplitudes. The first few peaks can be fit extremely well by these models. Adding noncircular variation can help bring the higher order peaks into line, as will be shown below, since, as one would expect, the smaller, higher order peaks are more sensitive to the small deviations from a cylinder that may be part of the real unit cell. The circular models do, however, demonstrate one of the advantages of $H_{II}$ geometry: the phasing of the peaks changes very slowly as the lattice swells, unlike the phasing of the lamellar phase. This is because the structure factor envelope moves along nearly with the peak positions, minimizing movement of the peaks across the structure factor nodes (see Figure 3).

Various models were analyzed to characterize the uncertainties inherent in limited resolution reconstructions. The amplitudes predicted by the model were transformed back to give the limited resolution model reconstruction. By varying the number of peaks included in the reconstructions, spurious series termination effects, such as the change in the location of the modeled phosphorus peak, could be examined. This procedure is equivalent to convoluting the true model electron density with the resolution function as described above. The phosphorus peak radius along a given radical direction is defined by the location of the maximum electron density observed along that radial slice. The position of this maximum depends on the resolution of the reconstruction since the resolution affects the fidelity of the reproduction (Figures 6

Table III: Comparison of Modeled Amplitudes with Measured Amplitudes at 20, 50, and 80 °C for DOPE

| order | model $F(q)$ | measured $\|F(q)\|$ |
|---|---|---|
| | DOPE at 20 °C, $d$ = 75.8 Å | |
| (1,0) | 0.891 | 0.885 |
| (1,1) | −0.949 | 0.922 |
| (2,0) | −0.700 | 0.759 |
| (2,1) | 0.153 | 0.200 |
| (3,0) | 0.289 | 0.229 |
| (2,2) | 0.183 | 0.162 |
| (3,1) | 0.128 | 0.131 |
| (4,0) | −0.005 | 0.001 |
| (3,2) | −0.068 | 0.091 |
| (4,1) | −0.074 | 0.102 |
| | $R = 4.8 \times 10^{-3}$ | |
| | DOPE at 50 °C, $d$ = 69.19 Å | |
| (1,0) | 0.973 | 0.972 |
| (1,1) | −0.856 | 0.841 |
| (2,0) | −0.688 | 0.714 |
| (2,1) | 0.053 | 0.094 |
| (3,0) | 0.204 | 0.159 |
| (2,2) | 0.158 | 0.170 |
| (3,1) | 0.125 | 0.142 |
| (4,0) | 0.040 | 0.027 |
| (3,2) | −0.013 | 0.017 |
| (4,1) | −0.031 | 0.024 |
| | $R = 2 \times 10^{-3}$ | |
| | DOPE at 80 °C, $d$ = 64.23 Å | |
| (1,0) | 1.002 | 1.002 |
| (1,1) | −0.764 | 0.756 |
| (2,0) | −0.647 | 0.660 |
| (2,1) | −0.029 | 0.002 |
| (3,0) | 0.122 | 0.088 |
| (2,2) | 0.133 | 0.146 |
| (3,1) | 0.117 | 0.134 |
| (4,0) | 0.060 | 0.046 |
| (3,2) | 0.007 | 0.000 |
| (4,1) | −0.017 | 0.000 |
| | $R = 1.5 \times 10^{-3}$ | |

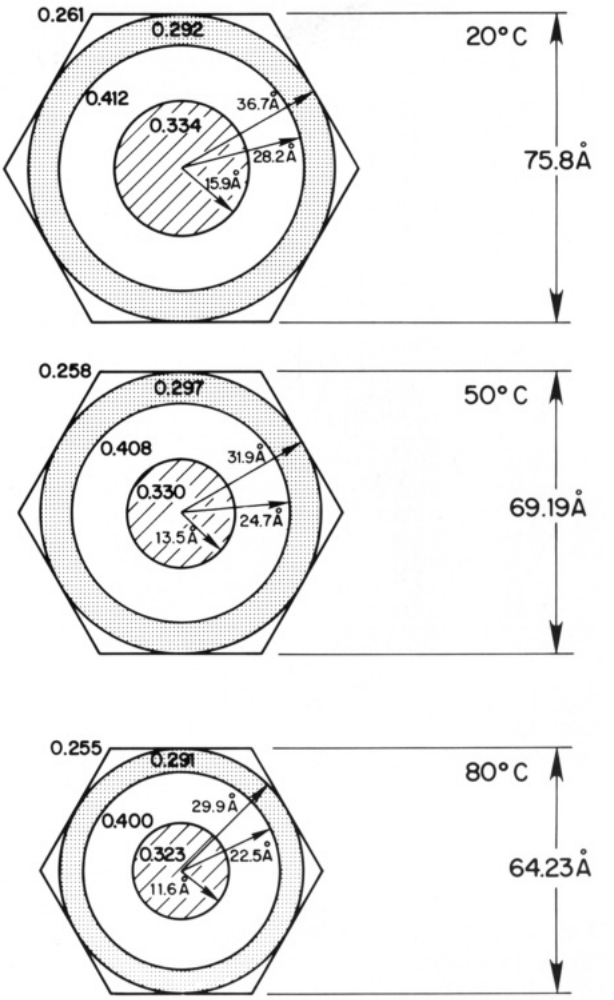


FIGURE 5: Best fitting cylindrical models to DOPE + excess water at 20, 50, and 80 °C. The structure factor amplitudes predicted by these models agree most closely with the experimental amplitudes (see the text and Table III).

and 7). The average of this value around the water core is defined to be the mean phosphorus radius, $R_p$. For 10 peaks, the modeled peak radius, $R_p$, is found to be offset from $R_{mod}$ by up to 0.5 Å but parallel to within 0.3 Å over the region of interest. The five- and seven-peak reconstructions are parallel to within 0.5 Å.

The measurement error for the real diffraction amplitudes is about 5% of the amplitude for the largest peak. It was, therefore, important to determine how such fluctuations are reflected in the reconstructed unit cell electron density to show how errors in the real data will propagate. Random (white noise) variations of this magnitude were introduced into the modeled amplitudes, specifically to examine their effect on the measured radius $R_p$. As an example, for a unit cell spacing of 74.81 Å, the modeled value of $R_p$ is 21.35 Å. The values of $R_p$ for several data sets with random noise in each are 21.1, 21.7, 21.5, and 21.4 Å. The noise added is 5% of the largest peak amplitude. These amplitude variations produced shifts of less than 0.5 Å from the ideal $R_p$'s.

The modeling results suggest that the phosphorus radius $R_p$ can be determined, up to a constant offset, to within 0.5 Å for the five- and seven-peak reconstructions over the range of unit cell sizes of interest. $R_p$ for the 10-peak reconstruction is parallel to the ideal to within 0.3 Å. The offset can be determined by comparison with previous data or from more sophisticated models when an accurate determination is required. The point to note is that the radius can be measured accurately to within a fraction of an angstrom even when the resolution of the reconstruction is very low, since for these reconstructions the resolution ($\Delta r$; see above) varies between about 17 Å for 10 peaks down to about 26 Å for 5 peaks.

Angular variations were also examined in the model reconstructions. The maximum and minimum phosphorus peak radii ($R_{max}$ and $R_{min}$) were determined as a function of angle for each reconstruction. The difference between the two extreme radii divided by the average radius, $R_p$, was defined to be the fractional water core shape variation, $\Delta R$. The maximum and minimum headgroup densities were also measured as a function of angle. The density variation along the headgroup peak contour, $\Delta\rho$, was defined to be $(\rho_{max} - \rho_{min})/\rho_0$, where $\rho_0$ is the average peak density of the headgroup region. Figure 8 shows plots of $\Delta R$ and $\Delta\rho$ for three different models: a circular water core model (Figure 4), a hexagonally shaped water core, and a circular headgroup with density ripple, plotted as a function of unit cell size for a 10-peak reconstruction. The reconstructions behave as expected, with the cylindrical model exhibiting small $\Delta R$ and $\Delta\rho$, the density ripple model exhibiting a small $\Delta R$ and a large $\Delta\rho$, and the hexagonal water core model showing an intermediate $\Delta\rho$ and a large $\Delta R$. These three extreme cases are easily distinguishable at this resolution. The real unit cell is expected to be a compromise between these different types of distortion, so the interpretation will be more complicated, particularly if the hexagonal distortions are small. In addition, these values are found to be sensitive to random errors in the diffraction amplitudes, so interpretation of the real data is more difficult

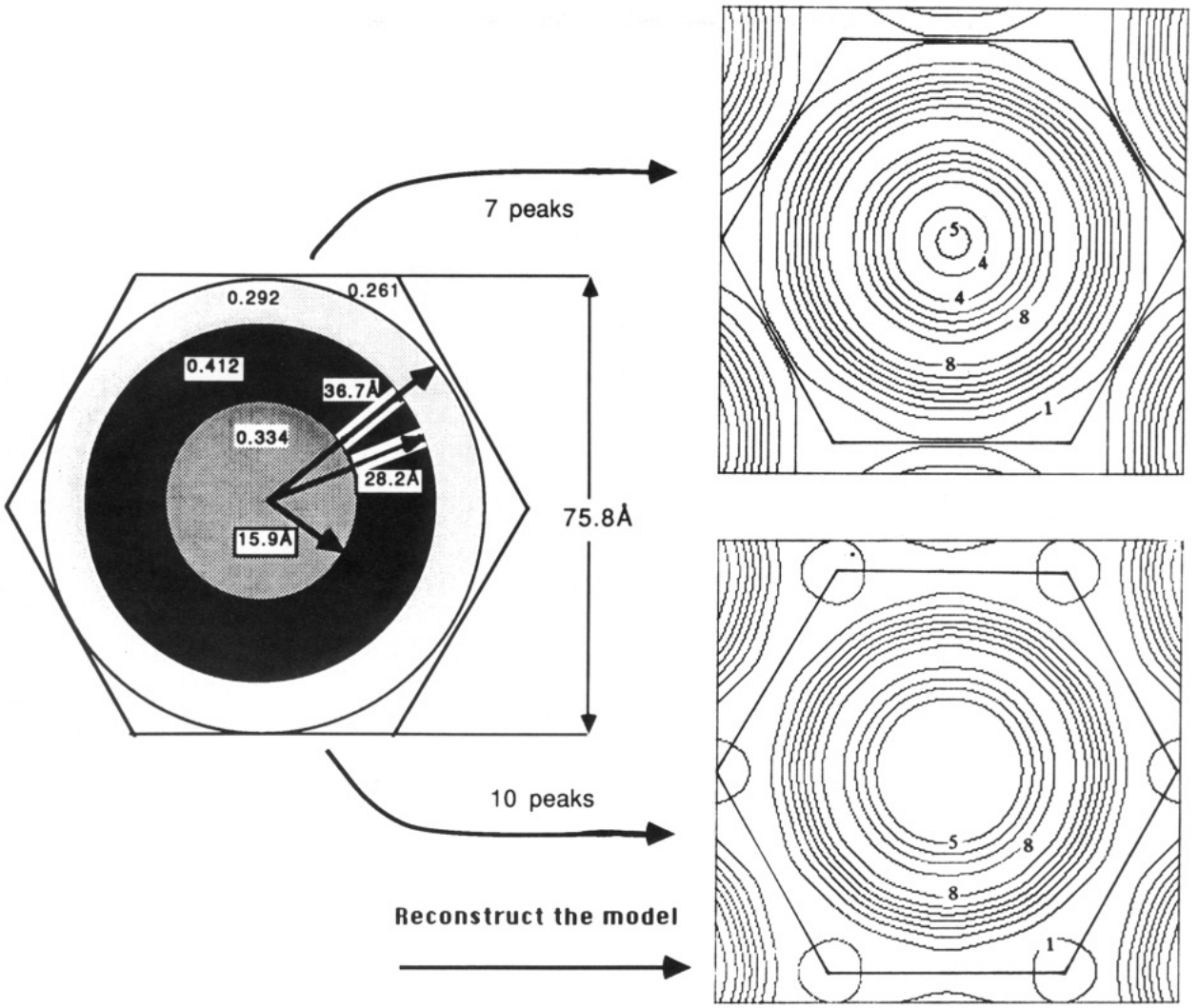


FIGURE 6: Reconstructions of a simple circular model when the resolutions are limited to 7 and 10 peaks of the hexagonal lattice transform. Here we see how prematurely terminating the Fourier series adds noncircular artifacts to a low-resolution reconstruction of a circular model, i.e., note the shape of the headgroup peak contour. It is precisely these artifacts which need to be calibrated before reconstructions of the real data can be quantitatively assessed.

than these plots suggest. Nonetheless, $\Delta R$ and $\Delta\rho$ will be useful at least as a semiquantitative way of estimating the variation from cylindrical symmetry for the real data.

The best fitting cylindrical models were modified by adding noncylindrical variation to determine the best overall model fit to the data. Each fit has a reduced $\chi^2$ of less than 1 when the mean error for each measured amplitude is taken to be ~5% of the largest amplitude. In particular, we define

$$R = \frac{\sum_{i,j}(|F_{ij}^{\text{model}}| - |F_{ij}^{\text{meas}}|)^2}{\sum_{i,j}(|F_{ij}^{\text{meas}}|)^2} \quad (8)$$

where $F_{i,j}$ are the $i,j$th modeled or measured peak amplitudes, as a measure of goodness of fit. The 50 and 80 °C DOPE + excess water data are fit well [$R \approx (0.75\text{–}1) \times 10^{-3}$] by a cylindrical water core with small headgroup density ripples (<2–5%). In contrast, when the 20 °C data were fit to a cylindrical water core model, the fit was relatively poor ($R \approx 5 \times 10^{-3}$). However, when the shape of the water core was modified to be the sum of a cylindrical part and a hexagonal part, the fit was as good ($R \approx 1.5 \times 10^{-3}$) as the circular water core fits at higher temperature. This suggests that when the lattice size grows with decreasing temperature, and $d_{\max} - d_{H_{II}}$ (Figure 1) grows, the actual shape of the interface becomes a compromise between a circle and a hexagon, particular along the chain–headgroup boundary (Figure 9). It is likely that chain packing stress is distorting the water core shape by pulling the headgroups toward the corner of the Wigner–Seitz cell along the [1,1] direction (see Figure 1).

*Internal Structure of DOPE + Excess Water.* Once the phasing is known, the internal dimensions of the actual unit cell can be easily determined as a function of temperature. Specifically, the average phosphorus peak radius ($R_p$) along with $R_{\max}$ and $R_{\min}$ can be determined from the diffraction amplitudes by the protocol described above. The models predict a phasing of +,–,–,+,+,+,+,+,–,– for the 10-peak reconstruction of DOPE + excess water at all temperatures below 70 °C. Above 70 °C the phase of the (2,1) peak changes to "–". Figure 10 shows the resulting electron density maps at 20 and 80 °C. At 20 °C the resolution of the reconstruction is 17 Å, while it is 15 Å at 80 °C. An important feature is the deep hole in the electron density near the interstitial region of the Wigner–Seitz cell along the [1,1] direction. This is the region where the lipid chains have to stretch furthest to fill space. This hole gets deeper as the temperature decreases and lattice size increases. A plausible explanation is that the low-density terminal methyl groups of each lipid chain are preferentially partitioning into those regions, particularly at low temperature. This may also be simply due to geometrical constraints as well, since this is the

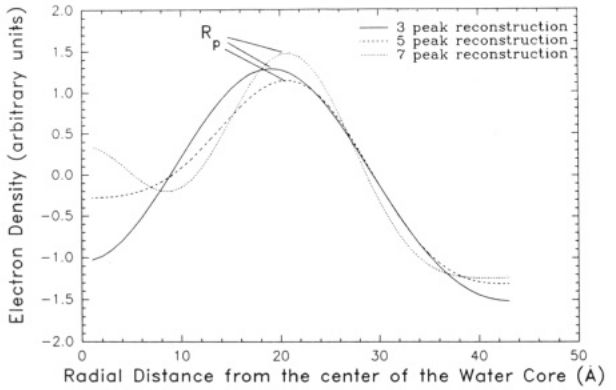


FIGURE 7: Changes in the reconstructed electron density radial profile with resolution. This figure shows radial slices (along the [1,1] direction) of circular model reconstructions (see Figure 4 for the model) for different number of peaks included in the reconstructions. The solid, dashed, and dotted lines correspond to the three-, five-, and seven-peak reconstructions, respectively. As the number of peaks included in the reconstruction is increased, the sharpness of the features improves, as can be expected from improving the resolution from 39 Å for the three-peak reconstruction to 22 Å for the seven-peak reconstruction. In addition, the position of the major features shifts with resolution. The maximum of the electron density is defined to be the radius of the phosphorus peak $R_p$. This position shifts dramatically between the three- and five-peak reconstructions but thereafter changes position (though not amplitude) only weakly with increasing resolution.

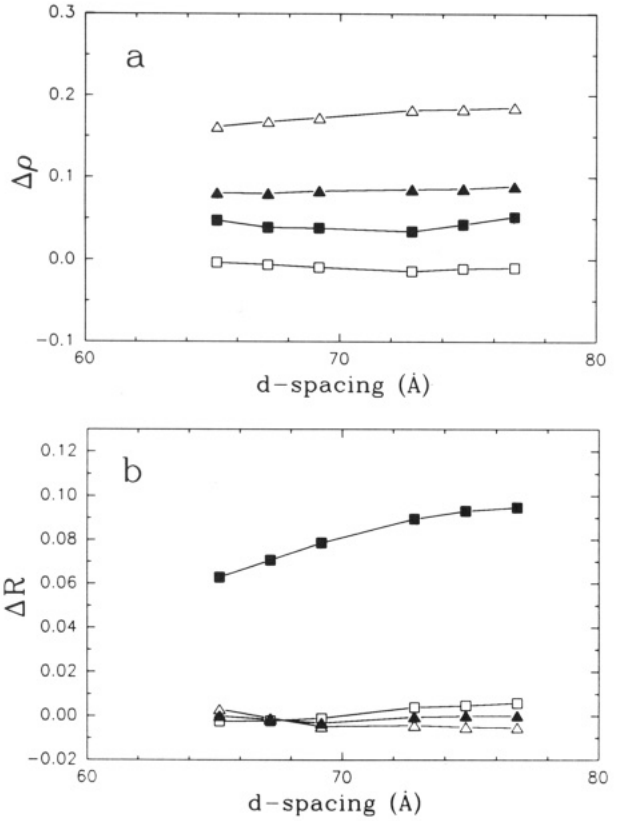


FIGURE 8: (a) Plot of $\Delta\rho$ vs $d$-spacing for four different models: circular water core (open square), hexagonal shape water core (filled square), 5% ripple in the headgroup density with high density along the [1,1] direction and low density along the [1,0] direction (filled triangle), and 10% density ripple in the headgroup (open triangle). All models are reconstructed with 10 peaks. As expected, the circular model shows a very small $\Delta\rho$, and the models with headgroup ripples have larger $\Delta\rho$. A hexagonally shaped water core shows a small but nonzero value for $\Delta\rho$. (b) Plot of $\Delta R$ vs $d$-spacing for the four different models. Since $\Delta R$ is a measure of radial shape variations around the central water core, the hexagonal model is expected to show the largest value of $\Delta R$. The other three models show almost no shape variation, as expected.

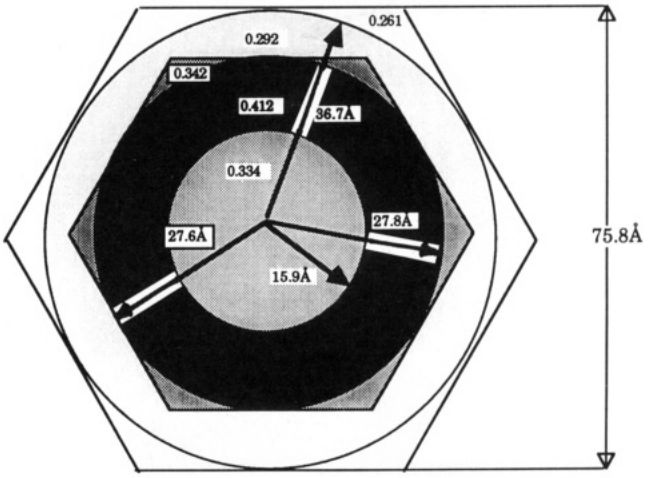


FIGURE 9: Best noncylindrical model fit to DOPE + water at 20 °C. A small hexagonal shape variation added to the outer edge of the modeled headgroup region improves the fit to the experimental amplitudes considerably.

only point that the terminal methyl groups from three adjacent unit cells can reach. This must not be oversimplified, however, since we are observing a time-averaged distribution rather than a static distribution within the unit cell.

Tate and Gruner (1989) have measured the average water core radius ($R_w$) as a function of temperature for the excess water phase of DOPE via traditional methods. Figure 11 shows their value of $R_w$ compared to $R_p$ from 5-, 7-, and 10-peak electron density reconstructions as a function of temperature. The 5- and 7-peak $R_p$'s agree with $R_w$ to within 0.7 Å. For 10 peaks, $R_p$ agrees with $R_w$ to within 0.5 Å. In fact, the electron density peak gives the location of the phosphorus so it should be slightly shifted from the value of $R_w$, with the difference being the distance from the average water core radius to the phosphorus position. Since the difference between these two radii is within 0.5 Å, the error of the measurement, the radius of the phosphorus position, $R_p$, will be used interchangeably with the radius of the water core $R_w$. The striking utility of the electron density map is now clear, with a single excess water sample, the radius of the water core, as defined by the circle which would smoothly partition the lipid and water mass, can be directly measured. The method used by Tate and Gruner (1989) requires preparing 10–15 samples of precisely determined composition, then allowing them to come to equilibrium over days or weeks. Excess water samples are easier to make and can be made to equilibrate relatively quickly, so the reconstruction method often saves a tremendous amount of time while providing more direct information regarding possible anisotropy in the unit cell. In fact, the radius of the water core $R_w$ can be used to determine the water volume fraction of the sample, $\phi_w$:

$$\phi_w = \frac{2\pi R_w^2}{\sqrt{3d^2}} \tag{9}$$

Assuming an error of 0.5 Å in both $R_w$ and $d$, the fractional error in the estimate for $\phi_w$ is 5.2%, which is good enough for many applications [see, for example, Narayan et al. (1990)].

The models described above imply that a 10-peak reconstruction is sufficient resolution to determine the shape of the water core. Figure 12a shows a plot of $R_{max}$ and $R_{min}$ vs temperature. The small difference between $R_{max}$ and $R_{min}$ indicates the accuracy of the cylindrical water core approximation. Figure 12b shows the lipid thickness along the [1,0] direction, $d_{H_{II}}$, and along the [1,1] direction, $d_{max}$, plotted vs temperature. Notice that $d_{H_{II}}$ and $d_{max}$ increase with de-

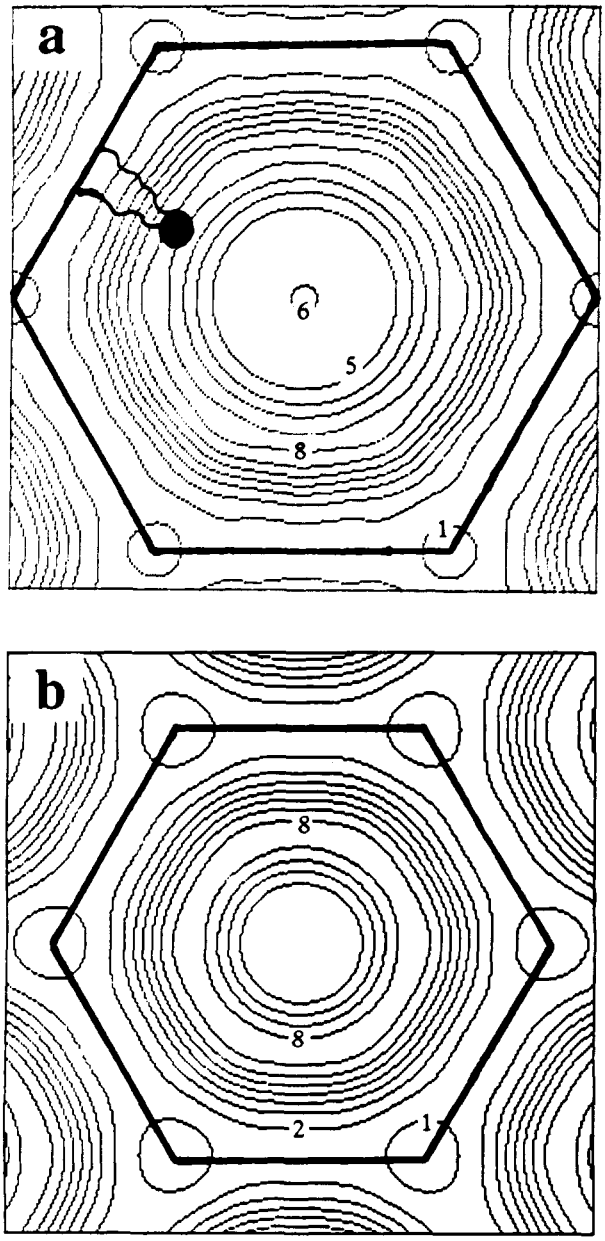


FIGURE 10: (a) Ten-peak electron density reconstruction of DOPE + excess water at 20 °C, $d$ = 75.8 Å, with a phasing +,−,−,+,+,+,+,+,−,−. (b) Ten-peak reconstruction of DOPE + excess water at 80 °C, $d$ = 64.23 Å, with a phasing +,−,−,−,+,+,+,+,−,−. The outline of the Wigner–Seitz cell and a prototypical lipid are drawn in to guide the eye.

creasing temperature, with $d_{max}$ increasing most rapidly. This difference of the lipid length between the [1,1] and [1,0] direction reduces the overall configurational entropy of the lipid chains and is probably driving the transition to the lamellar phase at low temperatures (Kirk et al., 1984).

Comparing $\Delta R$ and $\Delta\rho$ for the real data to the model above can establish the type of deviations from a cylinder that exist. Figure 13a shows a plot of $\Delta R$ vs temperature and Figure 13b a plot of $\Delta\rho$ vs temperature. As mentioned above, both of these values are very sensitive to the amplitudes of the weak higher order reflections in the diffraction pattern, i.e., $\Delta R$ and $\Delta\rho$ sample the higher frequency terms in the Fourier series. As a result, the error bars are large and were estimated by adding noise of the magnitude of the errors in the real diffraction amplitudes to the model systems and observing the effects on $\Delta R$ and $\Delta\rho$. This procedure is equivalent to reconstructing the real data with its associated errors because the Fourier

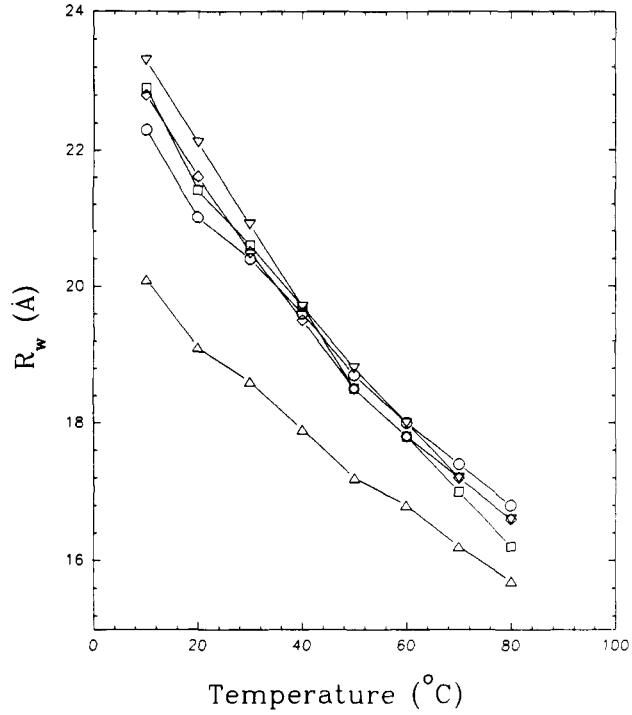


FIGURE 11: Temperature dependence of the radius of the phosphorus peak, $R_p$, for 3-, 5-, 7-, and 10-peak reconstructions (up triangle, square, circle, and down triangle) of DOPE + excess water, compared to the measured radius of the water core, $R_w$ (diamond), from Tate and Gruner (1989). As mentioned in the text, the 10-peak radius agrees with Tate and Gruner to within 0.5 Å. Since the error of the measured radius is 0.5 Å for both the 10-peak radius (from modeling) and Tate and Gruner's value, we will use $R_p$ and $R_w$ interchangeably to describe the radius of the water core and the radius of the phosphorus peak.

transform is a linear operator. The large errors are a reflection of the scatter of peak amplitudes over many data sets; however, for any single sample, the relative errors will be smaller as a function of temperature because random errors will dominate rather than systematics. This is evidenced by the smoothness of the curves generated for each data set. All data sets show a clear increase in $\Delta R$ as the lattice size increases. For the data shown (an average case), it increases to 0.03 as the temperature is reduced to 10 °C, which corresponds to a 5–10% radial shape deformation in the lipid–water interface (see Figure 8). On the other hand, $\Delta\rho$ remains between 0.0 and 0.1 over the full temperature range, corresponding to less than a 5% density ripple when compared to the model data. Both of these conclusions are consistent with the best fit models described above.

Such deviations from a cylinder suggest that the lattice is under curvature stress. Deviations from a cylinder add points of high local monolayer curvature which is likely to be energetically unfavorable form the standpoint of headgroup–headgroup interactions while also being entropically unfavorable. Such a deformation must be a reaction to another stress in the system, which in this case appears to be an entropic chain anisotropy. The chains are distorting the lipid–water interface in an attempt to pack more uniformly. This particular effect can be examined more closely by reducing the packing stress in the unit cell through the addition of certain free hydrocarbons to the system.

*DOPE + Added Hydrocarbon.* To obtain the same resolution as the electron density reconstructions of DOPE + excess water, 10 diffraction orders were collected for each sample of DOPE + dodecane or squalene. The diffraction patterns observed are qualitatively similar to the pure DOPE patterns and have similar measurement errors. The higher

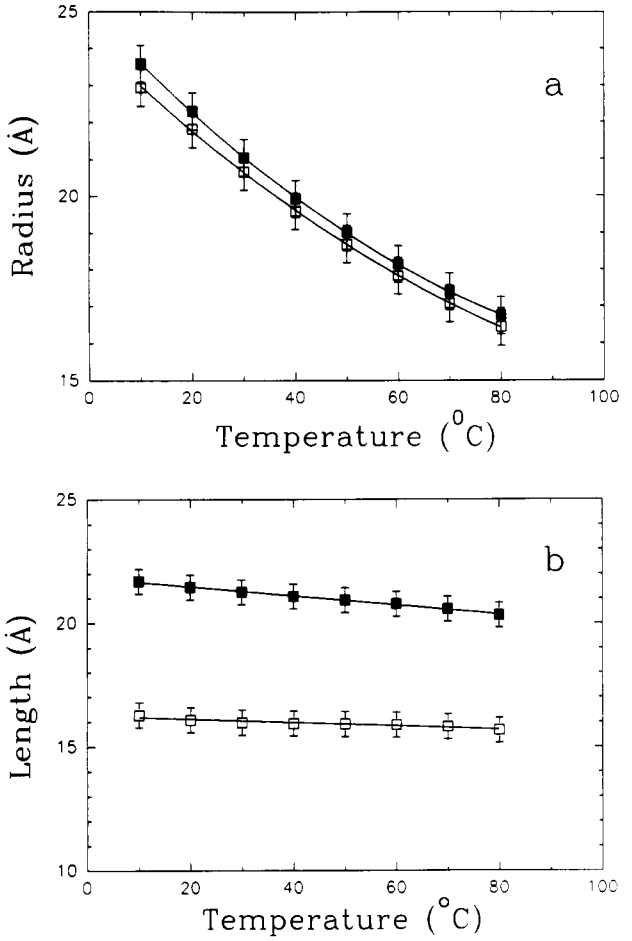


FIGURE 12: (a) Plot of $R_{max}$ (open square) and $R_{min}$ (filled square) vs temperature for a 10-peak reconstruction of DOPE + excess water. These are the maximum and minimum phosphorus radii measured around the central water core. $R_{max}$ and $R_{min}$ correspond to roughly the position of the phosphorus peak of the headgroup. It should be near the middle of the band of electron density representing the headgroup region in the model of Figure 5. Notice that their difference, $\Delta R$, grows upon cooling (see Figure 13a). (b) Maximum, $d_{max}$ (filled square), and minimum, $d_{H_{II}}$ (open square), lipid length vs temperature, as calculated from a 10-peak reconstruction of DOPE + excess water. See Figure 1a for a definition of $d_{max}$ and $d_{H_{II}}$ under the assumption of a circular water core. Here the distances reflect corrections due to noncircularities in the shape of the water core, i.e., $R_{max}$ and $R_{min}$. Notice that $d_{max}$ decreases more strongly with temperture than $d_{H_{II}}$, principally the result of a geometric amplification factor.

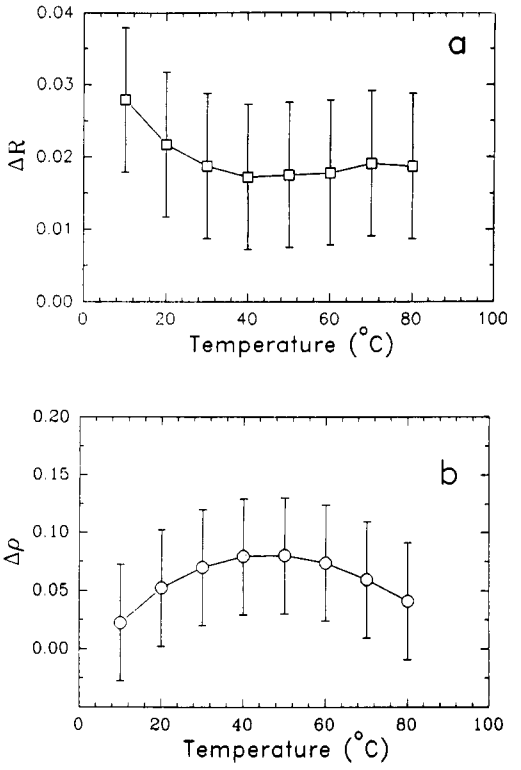


FIGURE 13: (a) A plot of $\Delta R$ vs temperature for DOPE + excess water using 10-peak reconstructions, where $\Delta R = (R_{max} - R_{min})/R_w$. Notice the strong increase with decreasing temperature, indicative of increasing noncircularities in the shape of the water core. (b) A plot of $\Delta\rho$ vs temperature for a 10-peak reconstruction of DOPE + excess water. $\Delta\rho$ is defined as $(\rho_{max} - \rho_{min})/\rho_{mean}$, where $\rho_{max}$ and $\rho_{min}$ are the maximum and minimum electron density found along the phosphorus peak as a function of angle and $\rho_{mean}$ is the average electron density in this region. This is a measure of electron density ripples in the region of the lipid headgroup. The concave shape of the curve is largely due to termination effects in the Fourier series. These values of $\Delta\rho$, however, are all consistent with less than 5% electron density ripples (compare with Figure 8).

order peaks, specifically the (4,0), (3,2), and (4,1) are very weak in some of these samples. In addition, they typically have a larger peak widths than the corresponding peaks seen for diffraction from pure DOPE. Both of these effects combine to increase the measurement uncertainty of the corrected high order peak amplitudes to 50–100%. This is probably due to less long-range spatial order [type II disorder; see Guinier (1963)] in the samples with free hydrocarbon. In fact, samples with fractions of dodecane greater than 16% were found to display weak, disordered diffraction. It appears that adding more alkane than this causes the lattice to lose some of its long-range positional order and may in fact induce the formation of another phase. No systematic study has been done on the effect of large fractions of alkane.

Table IV shows a list of the *d*-spacings and diffraction amplitudes for all of the hydrocarbon samples. The amplitudes of each data set were normalized to the (1,0) peak at 80 °C and smoothed by fitting to a quadratic function of temperature as for the pure DOPE data. Figure 14 shows a plot of *d*-spacing vs temperature for all of the samples including pure DOPE. The addition of either dodecane or squalene was observed to increase the *d*-spacing [see also Turner (1990) for a discussion of tetradecane and pentane]. It was found that the *d*-spacings for a given sample can fluctuate by as much as ±0.5 Å over and above the measurement uncertainty in the apparatus, even when the samples have similar thermal histories and have been equilibrated for periods up to a week. As such, equilibration of these samples is particularly difficult, especially with high concentrations of hydrocarbon. Both of these hydrocarbon molecules are effective in reducing the transition temperature to the $H_{II}$ phase ($T_{bh}$). Squalane, the saturated analogue of squalene, is known to be exceedingly effective in very small quantities (Siegel et al., 1989).

The first seven diffraction orders were phased using the swelling method, resulting in the phasing +,–,–,+,+,+,+. The peak amplitudes change smoothly with added alkane, so the phasing can also be inferred from the change in peak amplitudes away from the pure DOPE case. This can be used as a consistency check on the phasing determined by the swelling method. In fact, for the first seven peaks it was found that the correct phasing can be predicted by knowing the ratio $R_w/d$. For $R_w/d > 0.258$ the proper phasing was always +,–,–,+,+,+,+, for $0.237 < R_w/d < 0.258$ the proper phasing was +,–,–,–,+,+,+, and for $R_w/d < 0.237$ the phasing was found to be +,–,–,–,–,+,+. Phase changes are tantamount to movement of the sampling reflections across the zero crossings of the continuous structure factor. The upper and lower

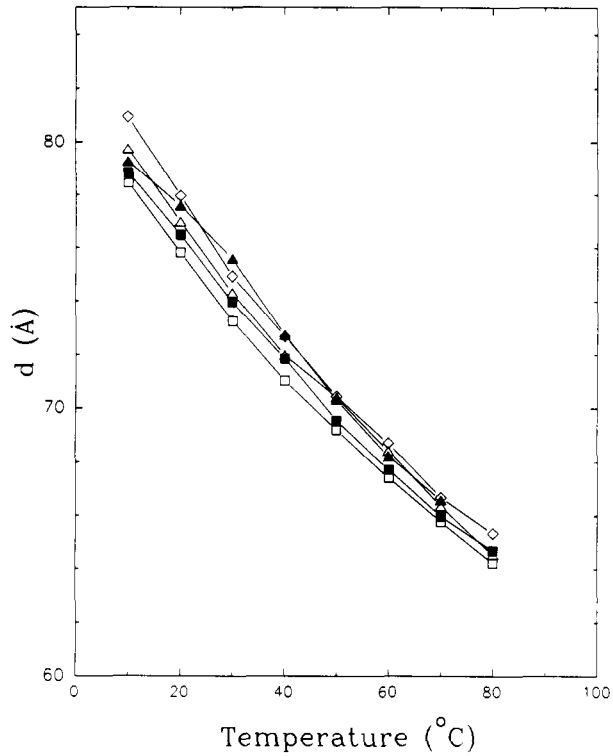


FIGURE 14: Plot of *d*-spacing vs temperature for DOPE + excess water and all of the DOPE samples with added hydrocarbon. Open square, filled square, open triangle, filled triangle, and diamond correspond to DOPE, DOPE + 5% dodecane, DOPE + 10% dodecane, DOPE + 16% dodecane, and DOPE + 10% squalene, respectively. All *d*-spacings are measured to ±0.5 Å.

bounds for the first and last cases have not been fully investigated. The weak, higher order peak phasings were inferred from the change in amplitude from the pure DOPE case and were compared to the phasing predicted by the best fit models. The most consistent phases for peaks (4,0), (3,2), and (4,1) for DOPE + 10% dodecane + excess water at 20 °C are +,–,–.

Models were fit to the diffraction amplitudes for all of the samples. Those with dodecane were best fit by a cylindrical water core model at all temperatures. The $R$ values for these fits are (2–2.8) × $10^{-3}$, with a trend toward better fits as the amount of dodecane is increased. The tendency toward a circular water core suggests dodecane and tetradecane's ability to relax hydrocarbon packing constraints; allowing the hydrocarbon tails to pack more uniformly frees the headgroups to relax to a uniform cylindrical shape. The 10% squalene sample also fits reasonably well to a cylindrical model ($R \approx 3 \times 10^{-3}$), although the fit can be improved by adding 2–5% headgroup density ripples. The significance of this additional circular anisotropy is not understood.

Figure 15 shows a reconstruction of DOPE + 10% dodecane at 20 °C with the phasing +,–,–,+,+,+,+,+,–,–. Although not evident in the figure, the electron density near the edge of the Wigner–Seitz cell is more uniform than that of pure DOPE. A more direct comparison of the electron density distributions for pure DOPE and DOPE + 10% dodecane is shown in Figure 16. Here the two data sets have been scaled such that the average electron density in the water region is the same and the electron density of the phosphorus peak is approximately the same for both samples. The two panels of the figure show radial sections of the electron density: one along the [1,0] direction, the other along the [1,1] direction (toward the corner of the Wigner–Seitz cell), with the two data sets plotted together for a direct comparison of their electron density profiles. The first obvious difference is the position

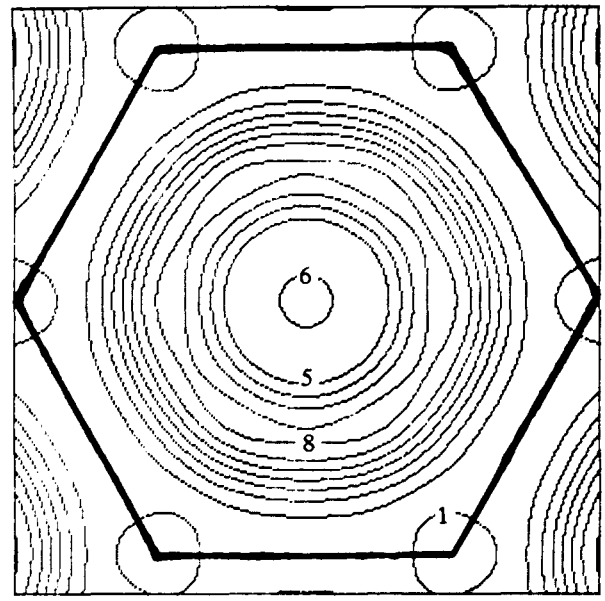


FIGURE 15: Ten-peak electron density reconstruction of DOPE + 10% dodecane + excess water at 20 °C, $d$ = 76.96 Å. The Wigner–Seitz cell has been drawn in to guide the eye.

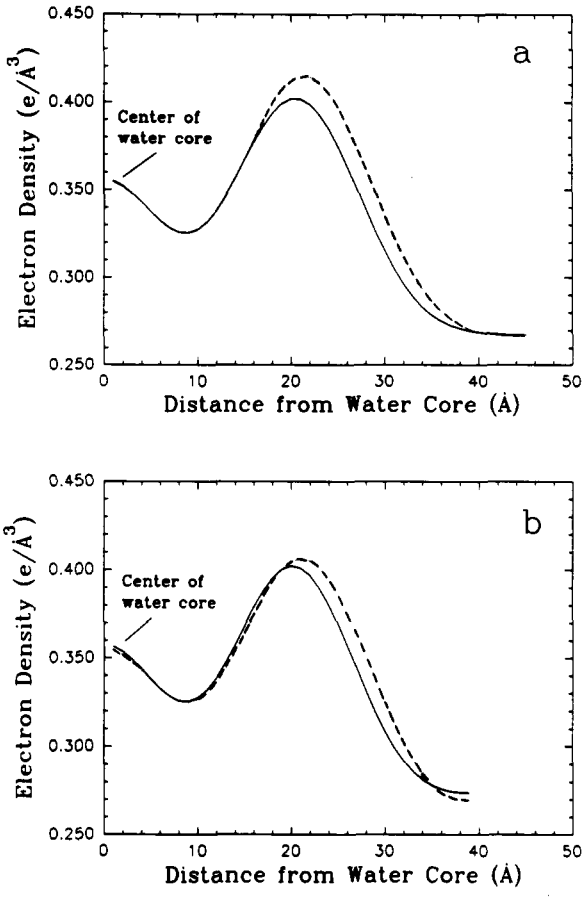


FIGURE 16: Electron density profiles along the (a) [1,1] and (b) [1,0] directions for DOPE + excess water (dashed line) and DOPE + 10% dodecane + excess water (solid line) at 20 °C. There are several points to notice in these figures. First, the headgroup electron density ripple seen in the pure DOPE sample has been virtually eliminated in the sample with 10% dodecane (compare maximum of panels a and b). Second, the position of the headgroup peak has shifted inward by about 1 Å for the sample with the added dodecane. Finally, the electron density near the edge of the Wigner–Seitz cell, i.e., at the terminal end of the lipid chains, is flattened out for the sample with added hydrocarbon when compared with the pure sample.

of the phosphorus peak: the water core radius with the added dodecane is reduced by approximately 1 Å. A more subtle

Table IV: Diffraction Amplitudes and *d*-Spacings for DOPE + Various Hydrocarbons

| | DOPE + 5% (w/w) Dodecane temp (°C)/*d*-spacing (Å) | | | | | | | |
|---|---|---|---|---|---|---|---|---|
| order | 80/64.69 | 70/65.97 | 60/67.71 | 50/69.54 | 40/71.85 | 30/73.96 | 20/76.48 | 10/78.81 |
| (1,0) | 1.001 | 0.984 | 0.961 | 0.939 | 0.912 | 0.889 | 0.863 | 0.841 |
| (1,1) | 0.630 | 0.641 | 0.658 | 0.679 | 0.708 | 0.736 | 0.773 | 0.808 |
| (2,0) | 0.553 | 0.564 | 0.579 | 0.595 | 0.614 | 0.631 | 0.651 | 0.669 |
| (2,1) | 0.027 | 0.016 | 0.009 | 0.013 | 0.029 | 0.053 | 0.093 | 0.137 |
| (3,0) | 0.027 | 0.047 | 0.072 | 0.096 | 0.124 | 0.146 | 0.169 | 0.188 |
| (2,2) | 0.155 | 0.161 | 0.168 | 0.174 | 0.180 | 0.185 | 0.189 | 0.191 |
| (3,1) | 0.123 | 0.131 | 0.139 | 0.146 | 0.151 | 0.154 | 0.154 | 0.153 |
| (4,0) | 0.063 | 0.057 | 0.049 | 0.040 | 0.029 | 0.017 | 0.004 | 0.000 |
| (3,2) | 0.000 | 0.000 | 0.000 | 0.000 | 0.002 | 0.012 | 0.029 | 0.047 |
| (4,1) | 0.000 | 0.000 | 0.000 | 0.000 | 0.006 | 0.017 | 0.033 | 0.052 |
| | DOPE + 10% (w/w) Dodecane temp (°C)/*d*-spacing (Å) | | | | | | | |
| order | 80/64.54 | 70/66.35 | 60/68.40 | 50/70.40 | 40/71.98 | 30/74.31 | 20/76.96 | 10/79.73 |
| (1,0) | 1.005 | 0.996 | 0.985 | 0.974 | 0.965 | 0.952 | 0.936 | 0.919 |
| (1,1) | 0.507 | 0.541 | 0.579 | 0.614 | 0.641 | 0.679 | 0.720 | 0.761 |
| (2,0) | 0.489 | 0.514 | 0.541 | 0.564 | 0.581 | 0.603 | 0.626 | 0.648 |
| (2,1) | 0.094 | 0.063 | 0.038 | 0.024 | 0.019 | 0.020 | 0.030 | 0.050 |
| (3,0) | 0.021 | 0.034 | 0.052 | 0.072 | 0.089 | 0.116 | 0.148 | 0.184 |
| (2,2) | 0.107 | 0.132 | 0.154 | 0.171 | 0.180 | 0.190 | 0.195 | 0.196 |
| (3,1) | 0.100 | 0.117 | 0.132 | 0.145 | 0.153 | 0.162 | 0.169 | 0.175 |
| (4,0) | 0.056 | 0.056 | 0.055 | 0.054 | 0.053 | 0.051 | 0.048 | 0.045 |
| (3,2) | 0.000 | 0.000 | 0.000 | 0.000 | 0.000 | 0.002 | 0.005 | 0.009 |
| (4,1) | 0.000 | 0.000 | 0.000 | 0.000 | 0.001 | 0.007 | 0.016 | 0.027 |
| | DOPE + 16% (w/w) Dodecane temp (°C)/*d*-spacing (Å) | | | | | | | |
| order | 70/66.57 | 60/68.21 | 50/70.31 | 40/72.75 | 30/75.58 | 20/77.57 | 10/79.24 | |
| (1,0) | 1.005 | 1.002 | 1.002 | 1.006 | 1.015 | 1.023 | 1.032 | |
| (1,1) | 0.472 | 0.502 | 0.539 | 0.578 | 0.619 | 0.647 | 0.668 | |
| (2,0) | 0.470 | 0.498 | 0.529 | 0.559 | 0.588 | 0.605 | 0.618 | |
| (2,1) | 0.113 | 0.107 | 0.096 | 0.080 | 0.056 | 0.037 | 0.020 | |
| (3,0) | 0.001 | 0.006 | 0.023 | 0.046 | 0.077 | 0.101 | 0.123 | |
| (2,2) | 0.138 | 0.135 | 0.137 | 0.146 | 0.166 | 0.183 | 0.201 | |
| (3,1) | 0.099 | 0.105 | 0.115 | 0.131 | 0.154 | 0.172 | 0.188 | |
| (4,0) | 0.109 | 0.107 | 0.105 | 0.102 | 0.099 | 0.096 | 0.094 | |
| (3,2) | 0.000 | 0.000 | 0.000 | 0.000 | 0.001 | 0.005 | 0.010 | |
| (4,1) | 0.000 | 0.000 | 0.000 | 0.000 | 0.000 | 0.000 | 0.000 | |
| | DOPE + 10% Squalene temp (°C)/*d*-spacing (Å) | | | | | | | |
| order | 80/65.34 | 70/66.67 | 60/68.69 | 50/70.44 | 40/72.69 | 30/74.93 | 20/77.95 | 10/80.95 |
| (1,0) | 1.003 | 0.981 | 0.949 | 0.922 | 0.889 | 0.858 | 0.817 | 0.780 |
| (1,1) | 0.654 | 0.674 | 0.702 | 0.724 | 0.749 | 0.772 | 0.798 | 0.820 |
| (2,0) | 0.595 | 0.612 | 0.632 | 0.646 | 0.661 | 0.670 | 0.679 | 0.682 |
| (2,1) | 0.000 | 0.006 | 0.026 | 0.045 | 0.074 | 0.104 | 0.149 | 0.195 |
| (3,0) | 0.081 | 0.100 | 0.128 | 0.151 | 0.178 | 0.203 | 0.234 | 0.262 |
| (2,2) | 0.162 | 0.174 | 0.188 | 0.194 | 0.198 | 0.197 | 0.188 | 0.174 |
| (3,1) | 0.134 | 0.149 | 0.164 | 0.170 | 0.169 | 0.160 | 0.139 | 0.110 |
| (4,0) | 0.000 | 0.000 | 0.000 | 0.000 | 0.000 | 0.000 | 0.000 | 0.000 |
| (3,2) | 0.016 | 0.009 | 0.007 | 0.013 | 0.028 | 0.052 | 0.094 | 0.130 |
| (4,1) | 0.037 | 0.039 | 0.045 | 0.052 | 0.065 | 0.081 | 0.106 | 0.133 |

effect (not illustrated) is the angular variation of electron density at the headgroup which is seen for the pure DOPE sample and absent in the sample with dodecane. The electron density near the end of the lipid chains is also seen to change between the two samples. Along the [1,0] direction the electron density in this region is increased slightly in the dodecane sample relative to the pure sample. This is a direct consequence of the increased electron density of the added alkane over the terminal methyl groups of the lipid chains. Either a small fraction of alkane is packing in this region or it simply has a small influence on the packing of hydrocarbon. More striking, however, is the change in the electron density profile along the [1,1] direction. Not only has the average density increased in this region, but the shape of the distribution has changed; the distribution seen for the dodecane sample is noticeably flatter. The dodecane makes the electron density distribution more uniform. In short, adding dodecane reduces the azimuthal variation within the unit cell. Both the change of the water core radius and the increase in electron density uniformity near the hydrocarbon tails will be discussed below, especially as they pertain to possible free energy changes in the system.

*Internal Dimensions of DOPE + Hydrocarbon Samples.* The average phospholipid headgroup radius, $R_w$, was computed for all of the samples and compared to pure DOPE. Figure 17 shows $R_w$ plotted vs temperature for all of the samples. There is a uniform trend to reduce $R_w$ as the weight fraction of dodecane increases. This effect may be due to a small fraction of dodecane intercalating between the hydrocarbon tails while the rest acts more like a bulk liquid near the end of the acyl chains. The size of the effect seems to correlate with the relative water solubility of the alkane, or more specifically with the relative partition coefficient between hydrocarbon and water, since pentane reduces the radius of the

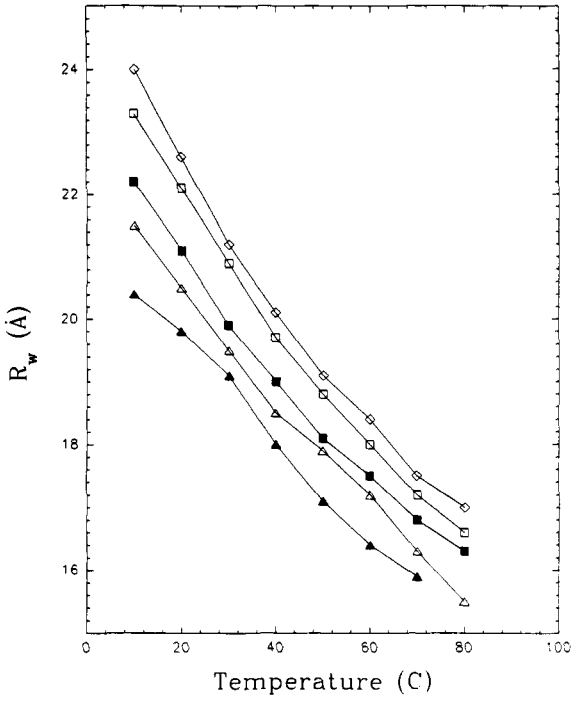


FIGURE 17: Radius of the water core, $R_w$, vs $d$-spacing for 10-peak reconstructions of DOPE + excess water and DOPE + excess water with added hydrocarbon. Open square, filled square, open triangle, filled triangle, and diamond correspond to DOPE, DOPE + 5% dodecane, DOPE + 10% dodecane, DOPE + 16% dodecane, and DOPE + 10% squalene, respectively. The precision of the measurement is ±0.5 Å. Dodecane lowers the radius of the water core, with the effect increasing with volume of hydrocarbon added. Squalene, on the other hand, increases the water core radius relative to the pure DOPE case.

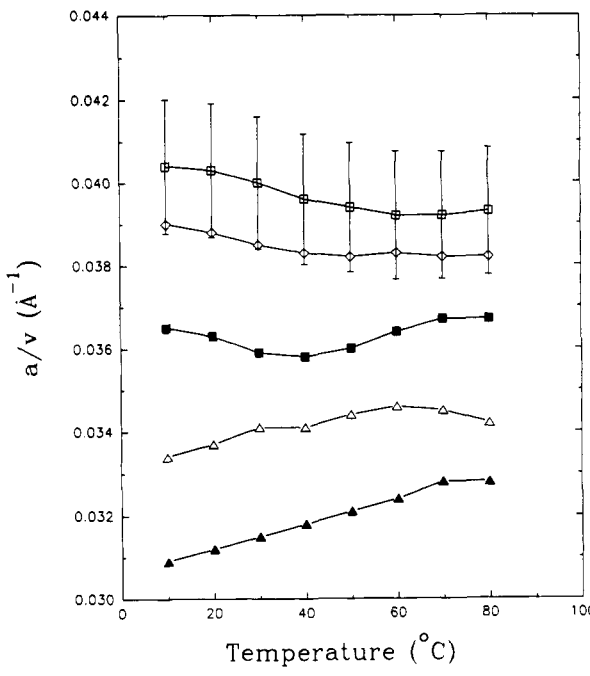


FIGURE 18: Plot of $a/\tilde{v}_l$ vs temperature for DOPE the hydrocarbon samples at excess water. Open square, filled square, open triangle, filled triangle, and diamond correspond to DOPE, DOPE + 5% dodecane, DOPE + 10% dodecane, DOPE + 16% dodecane, and DOPE + 10% squalene, respectively. Within error, $a/\tilde{v}_l$ for the pure DOPE sample remains constant with temperature, in agreement with the results of Tate and Gruner (1989). The added hydrocarbon appears to lower $a/\tilde{v}_l$, for a variety of possible reasons as explained in the text.

water core dramatically (Turner, 1990). As an aside, we note that Gruen predicts just such a length dependence for the packing of alkanes in lamellar monolayers: the short chains intercalate between the lipid chains while long chains pool near the terminal methyl groups at the center of the bilayer (Gruen, 1981). One would predict, therefore, that very long bulky chains of hydrocarbon would be excellent at reducing azimuthal lipid chain packing anisotropy. If we assume that in the absence of packing stress the monolayer will curl to some spontaneous radius of curvature, $R_0$, then the expressed radius of curvature of the water core should be below $R_0$ when under packing stress in the $H_{II}$ phase because the packing anisotropy increases with increasing lattice size. This implies that an ideal packing stress reducing compound will increase the water core size, i.e., it would relieve packing stress while allowing the radius of the water core to relax to its spontaneous radius. Unfortunately, long-chain alkanes (>16 carbons) are not suitable for this purpose because they are solid at room temperature. The highly branched polyisoprenoid squalene appears to be a good candidate. Unlike alkanes, 10% squalene appears actually to increase the radius of the water core, perhaps by allowing it to relax closer to its true spontaneous curvature. The increase in radius is about 0.6 Å at 20 °C. Along with its effectiveness in inducing the $H_{II}$ phase, the weak positive effect on water core radius suggests that squalene may be very close to the ideal packing stress reducing compound.

The area per lipid headgroup, $a$, can be calculated from the geometry of the phase to be

$$\frac{a}{\tilde{v}_l} = \frac{2}{R_w} \frac{1}{\frac{\sqrt{3}}{2\pi}\left(\frac{d}{R_w}\right)^2 - 1} \qquad (10)$$

where $\tilde{v}_l$ is the effective specific mean volume of lipid with its associated dodecane or squalene. Figure 18 shows $a/\tilde{v}_l$ plotted vs $d$-spacing for all of the samples. For pure DOPE, the value of $a/\tilde{v}_l = 0.040 \pm 0.002$ Å$^{-1}$ is only weakly dependent on temperature and within error is consistent with the value obtained by Tate and Gruner (1989). In the presence of dodecane, $a/\tilde{v}_l$ decreases with increasing weight fraction. This can be due to either the average area per headgroup decreasing or $\tilde{v}_l$ increasing. At 20 °C, the volume per molecule of dodecane is 369 Å$^3$ and the volume of a single DOPE molecule is 1230 Å$^3$.[2] A 5% weight fraction of dodecane corresponds to 18.7 mol %, so, assuming a linear addition of volumes

$$\tilde{v}_l = 1230 + \left(\frac{0.187}{0.813}\right)369 \text{ Å}^3 \qquad (11)$$

an increase of 6.9% over pure DOPE. The observed value of $a/\tilde{v}_l$ decreases about 10% when 5% dodecane is added. So most of the decrease in $a/\tilde{v}_l$ can be traced to the increase in effective lipid volume due to the added dodecane. When the same calculation is made for the addition of 10% dodecane the agreement is even better: $\tilde{v}_l$ increases by 14.5% while $a/\tilde{v}_l$ is found to decrease by about 15%. The results for tetradecane are similar. This means that the area per lipid headgroup, $a$, is apparently only weakly affected by the addition of dodecane.

When 10% squalene is added to DOPE, the effective volume per lipid should increase by 13%, while, in fact, the decrease in $a/\tilde{v}_l$ is found to be less than 2%. It is possible to explain this discrepancy by assuming that all of the squalene added to the sample does not fully partition into the lipid aggregate.

[2] Molecular volumes were calculated from the bulk density and molecular weights of DOPE (Tate, 1987; Dean, 1985) and dodecane (Weast, 1974).

The $R_w$ and $d$-spacing data shown in Figures 14 and 17 support this hypothesis: given $R_w$ and $d$ for pure DOPE, and $R_w$ and $d$ for the sample with squalene, we should be able to estimate the actual volume of squalene within the phase. The following conservation of volume equation should approximately hold:

$$(1 + \phi)\left(\frac{\sqrt{3}}{2}d^2 - \pi R_w^2\right) = \left(\frac{\sqrt{3}}{2}d'^2 - \pi R'^2_w\right) \quad (12)$$

where $\phi$ is the calculated volume fraction of squalene within the phase and the primes indicate the $d$ and $R_w$ values for the sample with added squalene. At 10 °C we have $d$ = 78.4 Å, $R_w$ = 24 Å, $d'$ = 81 Å, and $R'_w$ = 23.3 Å. Plugging in and solving for $\phi$, we find $\phi$ = 0.07. This compares to $\phi$ = 0.129 calculated directly from the known 10% weight fraction and the density (Weast, 1974). This implies that almost half of the squalene may not have partitioned into the lipid aggregate. This calculation, while crude, suggests that extreme care must be taken when interpreting deuterium NMR order parameter profiles for compounds of this type, particularly where isotropic peaks are observed, because the peaks may arise from bulk, phase-separated squalene. An attempt to measure the limiting fraction for squalene would be one way of testing this for example, by tracking changes in the $H_{II}$ diffraction vs overall squalene fraction. Such an experiment has yet to be done.

The lengths $d_{H_{II}}$ and $d_{max}$ (Figure 1) increase in length with volume of added alkane or squalene. If the reduction in $R_w$ is accounted for, the increase in $d$-spacing can be roughly attributed to an increase in the lipid volume due to the additional free hydrocarbon for the alkane samples. This leads to an increase in the measured values of $d_{H_{II}}$ and $d_{max}$ which can be reasonably well described by adding the effective volume of the free alkane to the end of the lipid acyl chains in the fashion of eq 12 above. As was shown above, the change in $d$-spacing with added squalene is not consistent with this assumption.

Since only the average change in lipid length can be derived, the specific angular distribution of lipid length cannot be deduced. Such an angular distribution of lipid lengths can only be determined if the distribution of alkane (or squalene) within the unit cell is known. When discussing the chain free energy within the phase, it is this distribution of lipid length which is important. In the accompanying neutron diffraction paper (Turner et al., 1992), the distribution of alkane within the unit cell was measured, from which the distribution of lipid lengths can be deduced. For the moment, it is noted that a likely measure of the hydrocarbon chain packing anisotropy is the uniformity of the electron density near the boundary of the Wigner–Seitz cell. Intuitively, one expects that a uniform packing environment would probably have uniform electron density. Such a conclusion is born out by observing the flattening of the electron density near the edge of the Wigner–Seitz cell with added dodecane, as shown in Figure 16 (described above).

This anisotropy can be examined by determining the mean square deviation from average density for a region of the Wigner–Seitz cell near the boundary, that is, by looking at the fluctuations in electron density near the ends of the lipid chains. The mean density $\rho_0$ was determined by averaging the electron density within this region near the Wigner–Seitz cell boundary. The deviation was then determined by summing $(\rho - \rho_0)^2/\rho_0^2$ over the whole region, where $\rho$ is the electron density at the point $(x,y)$. The region was defined as the area near the edge of the Wigner–Seitz cell which corresponds to a fraction $\delta$ of the total lipid area within the unit cell. The resulting sum is plotted vs temperature in Figure 19, where

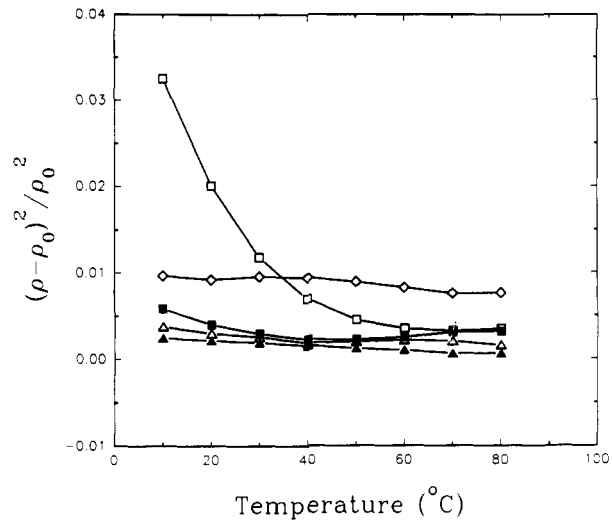


FIGURE 19: Plot of the deviation of $\rho$ near the end of the lipid chains vs temperature for DOPE and all of the hydrocarbon samples at excess water. Open square, filled square, open triangle, filled triangle and diamond correspond to DOPE, DOPE + 5% dodecane, DOPE + 10% dodecane, DOPE + 16% dodecane, and DOPE + 10% squalene, respectively. Specifically, this plot shows an integral of $(\rho - \rho_0)^2/\rho_0^2$ over a region near the edge of the Wigner–Seitz cell, where the size the of the region is determined to be a fraction, $p$, of the lipid volume within the unit cell. In this example $p$ = 0.02. This deviation is a measure of the nonuniformity of the electron density near the end of the lipid chains. The calculated value for the pure DOPE + excess water sample increases rapidly with decreasing temperature, while the hydrocarbon values generally remain flat as the temperature is decreasing.

$\delta$ has been taken to be 0.02, or 2%, of the lipid area; however, the characteristic shape of the curve is unchanged for any $\delta$ less than 0.10. The obvious feature of this plot is its dramatic increase for pure DOPE with decreasing temperature, while the values for dodecane remain relatively constant and below the pure DOPE curve. A uniform electron density may mean a more uniform packing environment for the lipid, thereby reducing the overall packing free energy. The squalene curve is intermediate to the pure DOPE and the DOPE + dodecane curves, indicating that it also promotes the $H_{II}$ phase by reducing packing anisotropies.

## Conclusion

This paper describes the application of low-resolution Fourier reconstructions of the $H_{II}$ phase to a structural examination of the packing of lipid and water within the phase. The phasing method described allows rapid determination of the signs of the peak amplitudes, often from a single sample. This is extremely useful because the internal dimensions of the unit cell, derived from the properly phase reconstruction, were shown to be in excellent agreement with the previous measurements done by Tate and Gruner (1989), so the reconstruction method can be used as a general tool for determining the water core radius and the lipid length within the unit cell. This simple result reduces the effort required to measure the internal dimensions of the $H_{II}$ phase at excess water by something like an order of magnitude. Perhaps more importantly, the reconstruction method yields a determination of the deviation from circular symmetry within the unit cell, in terms of the water core shape, azimuthal density variations of the headgroup peak, and the packing of hydrocarbon. For pure DOPE + excess water samples, we find that the water core shape begins to deviate from a circle as the lattice size is increased beyond ~75 Å. This is apparently due to the anisotropic hydrocarbon packing stress in the $H_{II}$ unit cell. The

resulting shape appears to be a compromise caused by the hydrocarbon stress competing with a curvature energy which would like to make the monolayer curvature uniform (Kirk et al., 1984).

The addition of small weight fractions of dodecane or squalene to a binary lipid–water mixture is known to promote the formation of the $H_{II}$ phase (Kirk & Gruner, 1985; Siegel et al., 1989). Kirk et al. (1984) suggested that these oils promote the $H_{II}$ phase by reducing the hydrocarbon packing stress within the phase. The structural studies in this paper are consistent with this suggestion: both dodecane and squalene relax the water core to a more circular shape while, at the same time, increasing the uniformity of the electron density (and probably the mass density as well) near the end of the lipid hydrocarbon chains. In a following paper in this issue, we present evidence via neutron diffraction that the alkane preferentially partitions into the interstitial region of the unit cell along the [1,1] direction (Figure 1a), where it can have the largest effect on improving the uniformity of the lipid packing environment as the X-ray diffraction data imply.

ACKNOWLEDGMENTS

D.C.T. thanks Dr. Mark Tate, Dr. E. Shyamsunder, Peter So, and Onuttom Narayan for useful discussions.

**Registry No.** DOPE, 4004-05-1; dodecane, 112-40-3; squalene, 111-02-4; water, 7732-18-5.

REFERENCES

Arfken, G. (1985) *Mathematical Methods for Physicists*, Academic Press, New York.

Buldt, G., Gally, H., Seelig, J., & Zaccai, G. (1979) *J. Mol. Biol. 134*, 673–691.

Cabane, B. (1986) in *Surfactant Solutions: New Methods of Investigation* (Zana, R., Ed.) Vol. 22, Marcel Dekker, New York.

Caron, F., Mateu, L., Rigny, P., & Azerad, R. (1974) *J. Mol. Biol. 85*, 279–300.

Cullis, P. R., Hope, M. J., de Kruijff, B., Verkleij, A. J., & Tilcock, C. P. S. (1985) in *Phospholipids and Cellular Regulations* (Kou, J. F., Ed.) Vol. I, pp 1–59, CRC Press, Boca Raton, FL.

Dean, J. A., Ed. (1985) *Lange's Handbook of Chemistry* McGraw Hill, New York.

Franks, N. P. (1976) *J. Mol. Biol. 100*, 345–358.

Franks, N. P., Melchior, V., Kirschner, D. A., & Caspar, D. L. (1982) *J. Mol. Biol. 155*, 133–153.

Gruen, D. W. R. (1981) *Biophys. J. 33*, 167–188.

Gruner, S. M. (1989) *J. Phys. Chem. 93*, 7562.

Gruner, S. M., Milch, J. R., & Reynolds, G. T. (1982) *Rev. Sci. Instrum. 53*, 1770–1778.

Guinier, A. (1963) *X-ray Diffraction*, Freeman, San Francisco.

Gulik, A., Luzzati, V., DeRosa, M., & Gambacorta, A. (1985) *J. Mol. Biol. 182*, 131–149.

Gulik, A., Luzzati, V., DeRosa, M., & Gambacorta, A. (1988) *J. Mol. Biol. 201*, 429–435.

Kirk, G. L., & Gruner, S. M. (1985) *J. Phys. (Paris) 46*, 761–769.

Kirk, G. L., Gruner, S. M., & Stein, D. E., (1984) *Biochemistry 23*, 1093–1102.

Knott, R. B., & Schoenborn, B. P. (1986) *Methods Enzymol. 127*, 217–229.

Luzzati, V. (1968) in *Biological Membranes* (Chapman, D., Ed.) Vol. 1, Academic Press, London.

Luzzati, V., & Husson, F. (1962) *J. Cell Biol. 12*, 207–219.

Milch, J., Gruner, S., & Reynolds, G. (1982) *Nucl. Instrum. Methods 201*, 43–52.

Narayan, O., So, P. T. C., Turner, D. C., Gruner, S. M., Tate, M. W., & Shyamsunder, E. (1990) *Phys. Rev. A 42*, 7479–7482.

Perutz, M. F. (1954) *Proc. R. Soc. London, A 225*, 264–286.

Press, W., Flannery, B. P., Teukolsky, S. A., & Vetterling, W. T. (1988) *Numerical Recipes in C*, Cambridge University Press, Cambridge.

Rand, R. P., Fuller, N. L., Gruner, S. M., & Parsegian, V. A. (1990) *Biochemistry 29*, 76–89.

Seddon, J. M. (1990) *Biochim. Biophys. Acta 1031*, 1–69.

Seddon, J. M., Cevc, G., Kaye, R. D., & Marsh, D. (1984) *Biochemistry 23*, 2634–2644.

Siegel, D., Banschbach, J., & Yeagle, P. L. (1989) *Biochemistry 28*, 5010–5019.

Sjolund, M., Lindblom, G., Rilfors, L., & Arvidson, G. (1987) *Biophys. J. 52*, 145–153.

Sjolund, M., Rilfors, L., & Lindblom, G. (1989) *Biochemistry 28*, 1323–1329.

Stamatoff, J. B., & Krimm, S. (1976) *Biophys. J. 16*, 503–516.

Tate, M. W. (1987) Ph.D. Dissertation, Princeton University, Princeton, NJ.

Tate, M. W., & Gruner, S. M. (1989) *Biochemistry 28*, 4245–4285.

Tate, M. W., Eikenberry, E. F., Turner, D. C., Shyamsunder, E., & Gruner, S. M. (1991) *Chem. Phys. Lipids 57*, 147–164.

Templer, R. H., Gruner, S. M., & Eikenberry, E. F. (1988) *Adv. Electron. Electron Phys. 74*, 275–283.

Torbet, J., & Wilkins, F. (1976) *J. Theor. Biol. 62*, 447–458.

Turner, D. C. (1990) Ph.D. Dissertation, Princeton University, Princeton, NJ.

Turner, D. C., Gruner, S. M., & Huang, J. (1992) *Biochemistry* (following paper in this issue).

Warren, B. E. (1969) *X-ray Diffraction*, Addison-Wesley, Reading, MA.

Weast, R. C., Ed. (1974) *CRC Handbook of Chemistry and Physics*, 55th ed., CRC Press, Cleveland, OH.

Weiner, M. C., Suter, R. M., & Nagle, J. F. (1989) *Biophys. J. 55*, 315–325.

Woolfson, M. M. (1970) *An Introduction to X-ray Crystallography*, Cambridge University Press, London.

Worthington, C. R. (1969) *Biophys. J. 9*, 222–234.

Worthington, C. R., King, G. I., & McIntosh, T. J. (1973) *Biophys. J. 13*, 480–494.